Description of Ion Properties Using Molecular Orbital Energy Levels

Sergey V. Doronin *

Posted Date: 23 July 2024

doi: 10.20944/preprints202407.1747.v1

Keywords: adsorption; binding; HOMO; LUMO; descriptors; ions; water; dymethyl cabonate; aliminium oxide; graphene; gold; aqueous electrolyte

Article

Description of Ion Properties Using Molecular Orbital Energy Levels

Sergey V. Doronin

N.N. Semenov Federal Research Center for Chemical Physics RAS, Kosygina Street 4, 119991, Moscow, Russia; sedoronin@gmail.com

Abstract: The study reveals correlations between the parameters of ions and their HOMO and LUMO orbital energy level values. In particular, it demonstrates a clear correlation for the ion adsorption parameters on model electrodes: the aluminum oxide (0001) surface, graphene and Au (111) surface. Correlations are also observed for the parameters of ion binding to water and dimethyl carbonate molecules, which are often used as solvents. In addition, the dipole moment, polarizability and solvation energy of ions are well correlated with the values of the molecular orbital energies, and for anions a dependence on the oxidation potential is observed. The obtained descriptors make it possible to select ions with desired values for a specific problem. As an illustrative example, in this work we consider the problem of displacement of water molecules from the inner electric double layer by ions, which is one of the factors increasing the potential window in electrolytes of aqueous batteries. This approach can be applied in the rapidly developing field of aqueous electrolytes for battery or supercapacitor design, catalysis control through surface composition variations, as well as in studies of heavy metal ion binding to sorption materials.

Keywords: adsorption; binding; HOMO; LUMO; descriptors; ions; water; dymethyl cabonate; aliminium oxide; graphene; gold; aqueous electrolyte

1. Introduction

The vast majority of activity parameters (descriptors) characterize the catalytic activity of heterogeneous catalysts. [1,2] Researchers have proposed a lot of electronic parameters that quite accurately describe the activity of various materials: centers of transition metal atomic bands, [3–5] orbital occupancy for transition metal oxides, [6] Fermi level, [7,8] effective coordination numbers [9] and associated electron density for metals, [10–12] density of states at the Fermi level for graphene, [13,14] etc. Such studies normally consider industrial reactions, for example, oxygen reduction, [14,15] hydrogen oxidation, [13,16] nitrogen fixation, [17,18] CO_2 conversion, [19,20] etc.

The activity parameters for molecules, [21–25] which are mainly used in molecular catalysis, design of biologically active substances, etc., are somewhat different. First and foremost in this list of parameters are the values of ionization potential (IP) and electron affinity (EA) and the associated energies of the highest occupied molecular orbital (HOMO) IP=-ε_{HOMO} and the lowest unoccupied molecular orbital (LUMO) EA=-ε_{LUMO}. [23] There are also a number of derived parameters based on HOMO and LUMO: [21–23] orbital energy difference ($\varepsilon_{HOMO-LUMO}$), chemical potential (μ), hardness (η), softness (S), electronegativity (χ), and global electrophility index (ω). These molecular descriptors find applications in catalysis, [21,24] corrosion studies, [25] evaluation of biological activity of compounds, [24] etc. In addition, complex descriptors for neutral molecules [26] and ions [26,27] were proposed for characterizing some parameters of complexes (dissociation constants, reaction rate constants, etc.). These parameters describe specific properties of complexes of molecules or ions based on a whole range of parameters of the system under study (dipole moment, molecular volume, hydrogen bonding strength, etc.).

 doi:10.20944/preprints202407.1747.v1

The vast majority of studies devoted to searching for activity descriptors usually consider a specific reaction proceeding on a variety of materials or active centers. [6,13–15,17–20] The main goal of such studies is to select materials on which the considered reaction has the highest rate. Despite the current trends, it is also appropriate to consider the reverse problem, where the study concerns the interaction of a variety of absorbents on the surface of one catalyst or molecule. Such studies can be extremely important for controlling the surface composition and surface activity of various applications in various industrial processes. In addition to catalysis, an example of an applied problem that can be solved is selection of the optimal electrolyte [28] for a particular electrode material in batteries or supercapacitors. Another practical application is binding of toxic impurities from solutions, especially binding of heavy metal ions. [29–31] Such descriptors will make it possible to evaluate the efficiency of a particular sorbent for a range of ions.

The existence of such descriptors is confirmed by the data of refs, [32–34] which show correlations of the adsorption energy of neutral molecules on the oxide surface with the HOMO and LUMO energy level and other parameters. Refs. [35,36] reveals correlations of the solvation energy with hardness. These facts suggest the possibility of a simplified description of the dependence of adsorption and some physicochemical and electrochemical parameters of molecules or ions on the energy level of the orbitals.

For better clarity and potential practical application, the present work analyzes the adsorption coupling of various ions on the surface of a dielectric (aluminum oxide (0001) surface), a semiconductor (graphene) and a metal (gold (111) surface). The intermolecular interaction is analyzed by studying the binding of water and dimethyl carbonate (solvents frequently used in chemical and electrochemical practice) to ions of molecules. Correlations between some physicochemical and electrochemical parameters of ions and their electronic structure are also analyzed. The systems under study are a number of surface inactive and active ions, which are used in electrochemical investigations of surface phenomena [37,38] and electron transfer, [37,39] organic electrochemistry [40–43] and potentially applicable in chemical current sources, [28,44–51] such as batteries, supercapacitors, etc.

2. Methods

Quantum-chemical calculations of ion adsorption on slabs were performed in the Quantum Espresso software package [52] within the generalized gradient approximation by the Perdew-Burke-Ernzerhof (PBE) functional [53] using standard PAW pseudopotentials. [54,55] Spin polarization was taken into account in the calculations and the maximum energy limit was 600 eV. The Monkhorst-Pack special point method [56] with an electron smearing of 0.1 eV and a k-grid density of 5x5x1 by the Methfessel-Paxton method [57] was selected for integration over the Brillouin zone. The energy convergence criterion of the self-consistent field method was set at 10^{-} [5] eV. The van der Waals interactions were considered within the Grimme method (DFT-D3). [58]

The relaxation of atoms in the slabs was carried out by the Broyden-Fletcher-Goldfarb-Shanno (BFGS) algorithm, the convergence criterion for the energy optimization of the atom geometry was set at 10^{-} [4] eV and the maximum force was 0.01 eV/Å.

A 72-atom graphene, a 60-atom Au(111), and a 60-atom α-Al_2O_3 (0001) slabs with cross-sectional dimensions of 6x6, 4x4, and 4x4 unit cells, respectively, were used as the model electrodes. The adsorption energy was calculated as the energy of the optimized slab with the ion on the surface minus the energy of the slab with the ion at a distance of 9–11 Å from the surface.

The cations in the study were the following systems contained in ionic liquids, [42,43] electrolytes for power sources, [48] including aqueous batteries that have been popular in the last decade, [28,47] as well as supporting electrolytes used in organic electrochemistry: [40,41] alkali metal cations (Li^+, Na^+, K^+, Cs^+, Rb^+), tetraalkylammonium cations R_4N^+ (R = -Me, -Et, -Pr, -Bu), derivatives of the pyridinium cation RPy^+ (R = -H, -Me, -Et), alkylmethylpyrrodilidone cation $RMPyr^+$ (R = -Et, -Bu) and alkylmethylimidazolium cation RMI^+ (R = -Et, -Bu, -Hexcyl (H), -Octyl (O), -Dodecyl (D), -Ph), cetyltrimethylammonium Me_3NCet^+ (CTA^+) and cetylpyridinium $CetPy^+$ (CP^+) cations.

 doi:10.20944/preprints202407.1747.v1

The anions were selected in a similar way: [47–49] OH^-, ClO_4^-, NO_3^-, and dycyanamide (DCA^-) grouped into a separate category for convenience; halides (F^-, Cl^-, Br^-); RSO_3^- derivatives (R = -NH_2, -Me, -Et, -Cet, -Ph) and HSO_4^- (R = -OH) added here; $RCOO^-$ carboxylates (R= -Me, -Et, -Pr, i-Pr and -Bu) and fluorine-containing anions (CF_3COO^-, tetrafluoroborate BF_4^-, hexaflurophosphate PF_6^-, trifluromethanesulfonate TfO^- and bis(triflurometh ylsulfonyl) imide $TFSI^-$).

In addition to the above systems, we considered the products of water autoprotholysis: hydroxide (OH^-) and hydroxonium (H_3O^+) ions.

The geometry optimization of ion complexes with water and dimethyl carbonate (DMC) molecules was carried out in the ORCA software package [59] with the B3LYP functional [60,61] and the 6-31++G(d,p) basis set. The free energy of ion-molecule binding was calculated as the difference between the free energy of the optimized aqueous complex and the original ions and water or DMC molecule in vacuum.

The dipole moment, polarizability, solvation energy and redox potential were calculated in the 6-311++G(3df,3pd) basis set. The solvation and redox potentials were determined within the PCM model [62–64] taking into account the dielectric parameters of the respective solvent; H_2O or DMC was used as the environment. The dielectric and other physical parameters of DMC for the PCM model construction were taken from refs. [65–67] For simplicity, the solvation energy (G_{solv}) was calculated as the difference between the free energy of the ion in the PCM model (G_{PCM}) and that of the ion in vacuum (G_{vac}): $G_{solv} = G_{PCM} - G_{vac} + G^{\circ\rightarrow *}$, where $G^{\circ\rightarrow *} = -k_B T \cdot \ln(24.4509)$ at T = 298 K is the term describing the process transition of the solute from gas 1 atm to solution 1 mole/L. The redox potential was calculated for the cations from the reduction reaction $Ion^+ + e^- = Ion$ [0] and for the anions from the oxidation reaction $Ion^- - e^- = Ion$ [0] as the difference between the energy of the initial ion ($G_{PCM}(Ion^{\pm})$) and that of the reduced or oxidized ion (GPCM(Ion0)): [28,68] $E_{pot} = -[G_{PCM}(Ion^+) - G_{PCM}(Ion\ [0])]/F$ or $[G_{PCM}(Ion\ [0]) - G_{PCM}(Ion^-)]/F$, where F was the Faraday constant. The absolute value of the redox potential (E_{pot}) was converted to a value relative to the standard hydrogen electrode (SHE): E_{pot} (vs. SHE) $= E_{pot} - 4.44$ V. [69] The values of the electronic levels of the ions were calculated by the B3LYP functional in the 6-311++G(3df,3pd) basis set in vacuum.

The distance between the center of mass of the ion and the surface (z_0) or the center of mass of the solvent molecule (r_0) was calculated using the Python library of the Atomic Simulation Environment (ASE). [70] A number of adsorbent and aqueous complex parameters, such as adsorption energies (E_{ads}), binding energies (G_{bind}) and distances (z_0 and r_0), were statistically averaged taking into account different conformations of the ions and solvent molecules.

3. Results and Discussion

3.1. Relation of Electronic Levels of Ions to Adsorption and Binding Energy

Let us evaluate how the energy level of an ion's orbitals can affect binding into an adsorption complex with solvent molecules or an electrode surface.

To consider the simplest scenario of the interaction of an ion with a solvent molecule through a one-electron operator, let us represent their wave functions in terms of Gaussian orbitals for a solvent molecule (assuming that the solvent consists of sufficiently light atoms) $\psi_{solv} = A_{solv} \cdot r^n \cdot \exp(-\alpha_{solv} \cdot r$ [2]), where n=0 for the s-orbital and n=1 for the p-orbital and $\psi_{ion} = A_{ion} \cdot r^n \cdot \exp(-\alpha_{ion} \cdot r$ [2]) for the s-, p- or d-orbital for the ion (n=2 for the d-orbital). A_{solv} and A_{ion} are normalizing coefficients, $\alpha_{solv} = 0.1$ a.u.$^-$ [2] and α_{ion} are exponential coefficients, and all the wave functions are normalized $\langle \psi_{solv} | \psi_{solv} \rangle = \langle \psi_{ion} | \psi_{ion} \rangle = 1$. The overlap of the wave functions is given by the expression $S = \langle \psi_{solv} | \psi_{ion} \rangle$.

The eigenvalues of the orbitals of the solvent molecule and ion [71,72] will look as follows:

$$\varepsilon_{solv} = \left\langle \psi_{solv} \left| \hat{H} \right| \psi_{solv} \right\rangle \quad \textbf{(1)}$$

$$\text{and} \quad \varepsilon_{ion} = \left\langle \psi_{ion} \left| \hat{H} \right| \psi_{ion} \right\rangle \quad \textbf{(2)}$$

 doi:10.20944/preprints202407.1747.v1

where

$\hat{H} = H_{kin} + H_{en} = -\frac{h^2}{2m_e}\nabla^2 + \sum_i \frac{e_0^2 q_i}{\varepsilon_0 |r - r_i|}$ is the one-electron perturbation operator, which is the sum of the electron kinetic energy (H_{kin}) and electron-nuclear interaction (H_{en}); ∇^2 is the Laplace operator; $|r - r_i| = \sqrt{(x - x_i)^2 + (y - y_i)^2 + (z - z_i)^2}$ is the distance between the electron density (product of the wave functions) at an arbitrary point x, y, z and a point charge q_i with x_i, y_i, and z_i coordinates of the i-atom; h is the Planck constant; m_e and e_0 are the mass and charge of the electron; ε_0 is the vacuum dielectric constant; i is the serial number of an atom in the solvent molecule.

The matrix element (V) for the orbitals is expressed through operator $\hat{H}$:

$$V = \left\langle \psi_{solv} \left| \hat{H} \right| \psi_{ion} \right\rangle \qquad (3)$$

The binding energy between the ψ_{solv} and ψ_{ion} orbitals is described by the expression: [4]

$$E_{bind} = 2\varepsilon_+ - \varepsilon_{solv} - \varepsilon_{ion} \qquad (4)$$

where ε_+ is the solution to the Schrödinger equation for the ground state,

$$\varepsilon_+ = \frac{(\varepsilon_{solv} + \varepsilon_{ion}) - \sqrt{4V^2 + (1 - S^2)(\varepsilon_{solv} - \varepsilon_{ion})^2}}{2(1 - S^2)} \qquad (5)$$

The energy level of the ψ_{ion} orbital can be changed by varying the α_{ion} parameter in the range of 0.001 – 0.5 a.u.$^{-}$ [2].

Now let us consider the adsorption of ions on the electrode using the Newnes-Andersen (NA) model. [3,73] According to the NA model, E_{ads} is determined by the sum of the contributions: [4,5,74,75]

$$E_{ads} = E_{hyb} + E_{ortho} \qquad (6)$$

The first term $E_{hyb} = \int_{-\infty}^{+\infty} \varepsilon f(\varepsilon)\rho_a(\varepsilon)d\varepsilon - 2\varepsilon_a$ represents the hybridization energy due to the overlap between the adsorbent orbitals and the electronic states of the electrode, the second term $E_{ortho} = -2(n_a + f)S|V_{ak}|$ is the orthogonalization energy (Pauli repulsion),

where f(ε) is the Fermi function, ε_a is the energy level of the adsorbent valence orbital, n_a is the filling of the adsorbent valence orbital determined by the expression $n_a = \int_{-\infty}^{+\infty} f(\varepsilon)\rho_a d\varepsilon$, and $f = \int_{-\infty}^{+\infty} f(\varepsilon)\rho_{el}d\varepsilon \Big/ \int_{-\infty}^{+\infty} \rho_{el}d\varepsilon$ is the degree of filling of the electrode electronic level.

For simplicity, we assume that V is proportional to $S = -\alpha \cdot |V|$, where α is a coefficient, and thus arrive at $E_{ortho} = 2(n_a + f)\alpha V_a^2$.

The density of states on the adsorbent is given by the expression

$$\rho_a(\varepsilon) = \frac{1}{\pi}\frac{\Delta^2(\varepsilon)}{(\varepsilon - \varepsilon_a - \Lambda(\varepsilon))^2 + \Delta^2(\varepsilon)} \qquad (7)$$

 doi:10.20944/preprints202407.1747.v1

where Δ and Λ are the chemisorption functions described by the expressions [76] $\Delta(\varepsilon)=\pi\sum_k|V_k|^2\,\delta(\varepsilon-\varepsilon_k)$, and Λ is the Hilbert transform of Δ: $\Lambda(\varepsilon)=\frac{1}{\pi}P\int\frac{|\Delta(\varepsilon')|}{\varepsilon-\varepsilon'}$, where *P* denotes the principal part. For simplicity, instead of the sum of values for all the k-vectors, we represent Δ(ε) in the form $\Delta(\varepsilon)\approx\pi\rho_{el}(\varepsilon)|V|^2$. [5,72,77]

The adsorbent nature in the NA model, eq. (**6**–**7**), is given directly only by parameters ε_a and V [2,5] S is indirectly related to the matrix element. In case of the ions, as the data show (Supplementary Material of ref. [72]) for O_2 and intermediates of oxygen reduction OH and OOH, the matrix element increases significantly due to the contribution of the electron-nuclear interaction. That is why we will evaluate the influence of, first of all, V [2] and then ε_a on E_{ads}.

Another way to estimate adsorption is to represent the effective orbital of an electrode as an s-function distributed along the z-axis perpendicular to the electrode, as in the jellium model: [78,79]

$$\psi_{el}=A_{el}\cdot\exp(-\alpha_{el}\cdot z\ [2]) \qquad \textbf{(8)}$$

Such approach has been used in numerous works [71,72,80–84] to estimate the matrix element of the overlap between the electrode and redox system orbitals. In the following calculations, α_{el} was set at 0.01 a.u.$^{-}$ [2] and the normalization factor A_{el} in (**8**) was calculated at the electrode surface (z=0) and at some distance from it using the expression $1=\int_{z=0}^{z=+\infty}\psi_{el}^2$.

In this method, the ψ_{el} function substitutes for ψ_{solv} in expressions (**1**–**3**). After that, all further calculations are made using equations (**4**, **5**), and the final expression for the adsorption energy can be rewritten as

$$E_{ads}=2\varepsilon_+-\varepsilon_{el}-\varepsilon_{ion} \qquad \textbf{(9)}$$

where $S=\langle\psi_{solv}|\psi_{ion}\rangle$, $\varepsilon_{el}=\left\langle\psi_{el}\left|\hat{H}\right|\psi_{el}\right\rangle$, $\varepsilon_{ion}=\left\langle\psi_{ion}\left|\hat{H}\right|\psi_{ion}\right\rangle$, $V=\left\langle\psi_{el}\left|\hat{H}\right|\psi_{ion}\right\rangle$ and the ground state energy $\varepsilon_+=\frac{(\varepsilon_{el}+\varepsilon_{ion})-\sqrt{4V^2+(1-S^2)(\varepsilon_{el}-\varepsilon_{ion})^2}}{2(1-S^2)}$.

The results of the calculations of binding of the orbitals of cations and anions with the solvent orbital using the model of eq. (**1**–**5**) give a set of graphs that fully or partially form two volcano-shaped dependencies (**Figure 1 A**, **B**). The graphs show that the orbital energies for the anions are mostly lower than those for the cations. It means that the centers of the volcano-shaped dependencies on the energy scale are shifted to the left for the anions and to the right for the cations.

In the regions of decreasing or increasing E_{bind} values, the graphs are quite close to linear or exponential dependencies. In case of s/s (schematic notation: solvent molecule orbital/ion orbital), s/p_z and s/d_{z^2} cation orbital interactions, the maximum region becomes sloped, which is caused by a large overlap of the orbitals due to their shape (σ-bond formation), lowering the binding energy value. When the solvent s-orbitals are combined with the d_{xy} and d_{xz} orbitals of the ions, rather weak π-bonds are formed. In case of the solvent p-orbitals, similar trends are observed for p_x/p_z and p_z/d_{z^2} and, to a lesser extent, for p_z/d_{xz} and p_x/p_x. The steeper slope of p_z/d_{xz} and p_x/p_x compared to s/p_x, etc. is explained by the larger extent of the p-orbital compared to the s-orbital, which results in a strong overlap and a decrease in the E_{bind} value. The specific shape of p_z/d_{z^2} is caused by the orientation of p_z-orbital directly towards the point charge of the ion. As a result, the contribution of the H_{ne} operator makes the bond stronger.

The most interesting trend is observed when the p_z-orbital of the anion participates in the binding, which causes a split in the left side of the branch (**Figure 1 A**, **B**). A special case are the results for the combination of s/s, and s/d_{z^2} orbitals at q=-1; p_x/p_x and p_x/p_y at q= -1 and p_x/p_x, p_x/p_y, and

Preprints.org (www.preprints.org) | NOT PEER-REVIEWED | Posted: 23 July 2024 doi:10.20944/preprints202407.1747.v1

p_z/d_{xy} at q= +1, for which stable solutions are obtained only for one of the branches, the shape of which is close to a linear function, and in some cases (s/d_{z^2}) to an exponential one.

The dependence of $E_{ads}(\varepsilon_a)$ according to the NA model, eq. (**6**, **7**), is almost linear and does not depend significantly on coefficient α (**Figure 1 C**), while in case of E_{ads}(V [2]) an exponential dependence is observed (**Figure 1 D**). In the region of moderately high values V [2]> 0.5 eV [2], the dependence of E_{ads}(V [2]) is almost linear. Notably, the approximation of specific results of DFT calculations of DOS adsorbents, for example, [74,75] shows that each bond type or band involved in the adsorption can have its own set of parameters ε_a and ε_c (band center). Therefore, for sufficiently high adsorption energies and, respectively, high V [2], the shape of the E_{ads}(V [2]) or $E_{ads}(\varepsilon_a)$ dependencies may become more complicated due to the contribution of a larger number of electrode bands and adsorbent orbitals involved in the adsorption process.

The calculations for the ions carried out by eq. (**9**) for the p_x, d_{xy}, $d_{x^2-y^2}$ orbitals lead to two volcano-shaped dependencies (**Figure 1 E**). Their side branches are close to linear dependencies and the interaction of the orbitals with the electrode is rather weak in this case. In case of the p_z and d_{z^2} orbitals, a quickly decreasing exponential dependence is observed. For the cations involving these orbitals, the E_{ads} dependence represents a function that decreases as the ε_{ion} value becomes higher. In general, this result is very close to the data obtained by the first model by eq. (**1**–**5**).

Since the HOMO or LUMO orbitals of real ions represent a superposition of a number of MOs, the total contribution of such composite orbitals to the final adsorption energy or energy of binding can become more complicated. If we consider the interaction between the solvent molecules and the ions, the dependence of the binding energy on the ion energy level becomes volcano-shaped. When the p-orbitals of the ion are oriented along the z-axis (perpendicular to the MO of the solvent molecule), the left side of the volcano-shaped E_{bind} dependence splits into two branches. In addition to the splitting, a scenario of parallel dependencies caused by the simultaneous contribution of multiple MOs of the ion is also possible. Within the NA model, the adsorption dependencies can be linear or exponential. However, if we consider the adsorption on the electrode through the effective wave function by eq. (**8**, **9**), we can expect the same trends as those obtained in the first model by eq. (**1**–**5**), i.e. formation of volcano-like dependencies or an exponential or linear decrease/increase in the adsorption energy.

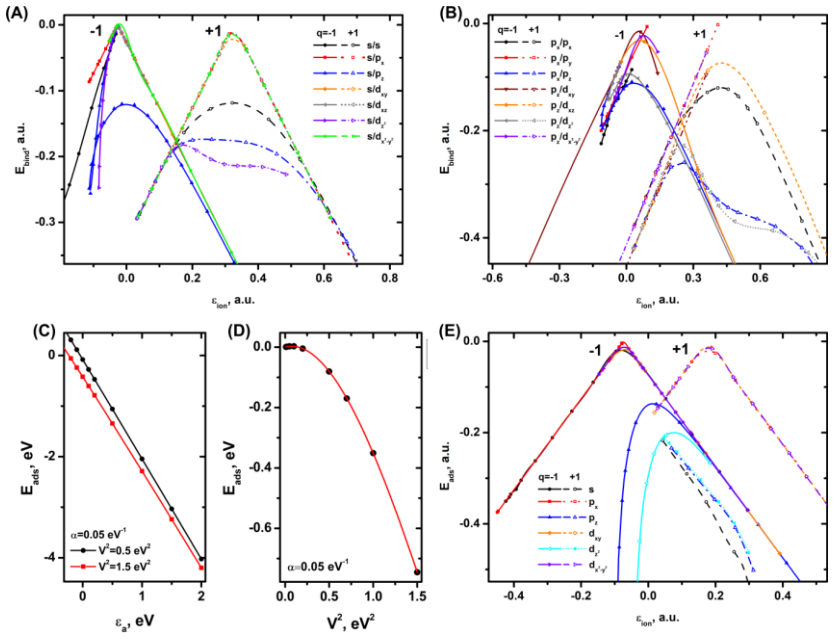

Figure 1. Dependence of the binding energy of cations (q=+1) and anions (q=-1) according to models (**1**–**5**) on their valence orbital energy level ε_{ion}. The solvent molecules are described by s- **(A)** and p_x- and p_z-orbitals **(B)**. Adsorption energy of the ions in the Newns-Andersen model according to

 doi:10.20944/preprints202407.1747.v1

equations (**6**, **7**) as a function of the energy level ε_a of the adsorbent **(C)** and the square of the matrix element V [2] **(D)**. Estimation of the adsorption energy of the ions by eq. (**9**) **(E)**.

3.2. Trends in Ion Adsorption on α-Al_2O_3 (0001), Graphene and Au (111)

Summarizing the data on the adsorption of ions (**Figure S1.1–S1.12**, **Table S2.3** in Supplementary Information) and their binding into complexes (**Figure S2.1–S2.4**, **Table S3.3**), we can conclude that it is most convenient to evaluate the energy levels of the HOMO (ε_{HOMO}) and LUMO (ε_{LUMO}) orbitals (**Table S4.1**, **S4.2**). In some cases, second highest (HOMO-1) and second lowest (LUMO+1) molecular orbitals can also be used. In addition, there are descriptors that combine HOMO and LUMO with HOMO-1 and LUMO+1 orbitals, e.g. hyperhardness or hypersoftness. [21] In case of strong correlations, combining parameters into descriptors may well make practical sense in some problems. Working directly with ε_{HOMO} and ε_{LUMO} levels allows us to describe the adsorption and distance from the electrode to the ion, avoiding additional calculations of descriptors made up of number of parameters. Therefore, we will mainly focus on the analysis of trends in adsorption and binding depending on one orbital only.

In case of Al_2O_3, quantum chemical calculations show that the value of the cation adsorption energy decreases exponentially (**Figure 2 A**) as the ε_{HOMO} value becomes lower and almost linearly when the ε_{LUMO} value goes down (**Figure 2 B**). The strongest binding to the surface is observed for alkali metal cations and H_3O^+ and the weakest binding for EMI^+. The distance from the electrode surface to the cation also follows the E_{ads} trends, where z_0 becomes lower as the ε_{HOMO} (**Figure 2 A**) and ε_{LUMO} (**Figure 2 B**) values decrease. Only H_3O^+ is slightly out of the general $E_{ads}(\varepsilon_{HOMO})$ trend, which may be caused by the formation of strong adsorption bonds between the hydrogen of H_3O^+ and the oxygen of the Al_2O_3 surface.

In case of $z_0(\varepsilon_{LUMO})$, only $PyMe^+$ does not follow the linear trend. Since the z_0 distance is determined at the ion center of mass, the elongated shape of the PyMe molecule and, consequently, the orbitals may cause overestimation of the z_0 value.

No correlation is observed between the anion adsorption and ε_{HOMO} (**Figure 2 E**), while in case of $E_{ads}(\varepsilon_{LUMO})$, there is a volcano-like dependence with a maximum at ε_{LUMO} = 0.245 a.u. (**Figure 2 F**). The strongest binding to the surface is observed for the $RCOO^-$, OH^-, and F^- systems, while that for the PF_6^- anion is the weakest. OH^- and F^- are out of the $E_{ads}(\varepsilon_{LUMO})$ trend, with the adsorption energies for the above ions getting as high as -4.0 and -4.3 eV, respectively; the adsorption energy in these cases is close to that of a strong chemical bond with the Al atoms.

The shape of $z_0(\varepsilon_{HOMO})$ and $z_0(\varepsilon_{LUMO})$ becomes more complicated (**Figure 2 G**, **H**), with the dependencies splitting into two curves that are reasonably well approximated by linear and exponential functions. In case of $z_0(\varepsilon_{HOMO})$, the linear dependence is formed by PF_6^-, BF_4^- and F^-, while the exponential one is represented by the other anions ($TFSI^-$, TfO^-; HSO_4^-, $MeSO_3^-$; ClO_4^-, NO_3^-, OH^-; $HCOO^-$, AcO^-, $EtCOO^-$ and Cl^-, Br^-). $z_0(\varepsilon_{LUMO})$ also splits into two dependencies, with the first linear one consisting of OH^-; HSO_4^-, $MeSO_3^-$; $HCOO^-$, AcO^-, and $EtCOO^-$ and the second exponential one represented by the $TFSI^-$, TfO^-, BF_4^-, PF_6^-; ClO_4^-, and NO_3^- anions and halides. In all the cases, z_0 decreases smoothly as the HOMO and LUMO energy values increase.

As the analysis (**Figure S1.13**) shows, the distance from the ions to the electrode surface for a number of systems correlates with the adsorption energy. For the anions, there is no $E_{ads}(z_0)$ correlation, while for the cations a linear dependence is observed (**Figure S1.13 A**, **B**).

It can be concluded that the adsorption of cations on aluminum oxide is the result of contributions of both the HOMO and the LUMO orbitals. The adsorption of the anions is determined by the LUMO, HOMO-1, and LUMO+1 levels (**B**, **D** in **Figure S1.1**, **S1.2**) and is independent of the HOMO one.

Preprints.org (www.preprints.org) | NOT PEER-REVIEWED | Posted: 23 July 2024 doi:10.20944/preprints202407.1747.v1

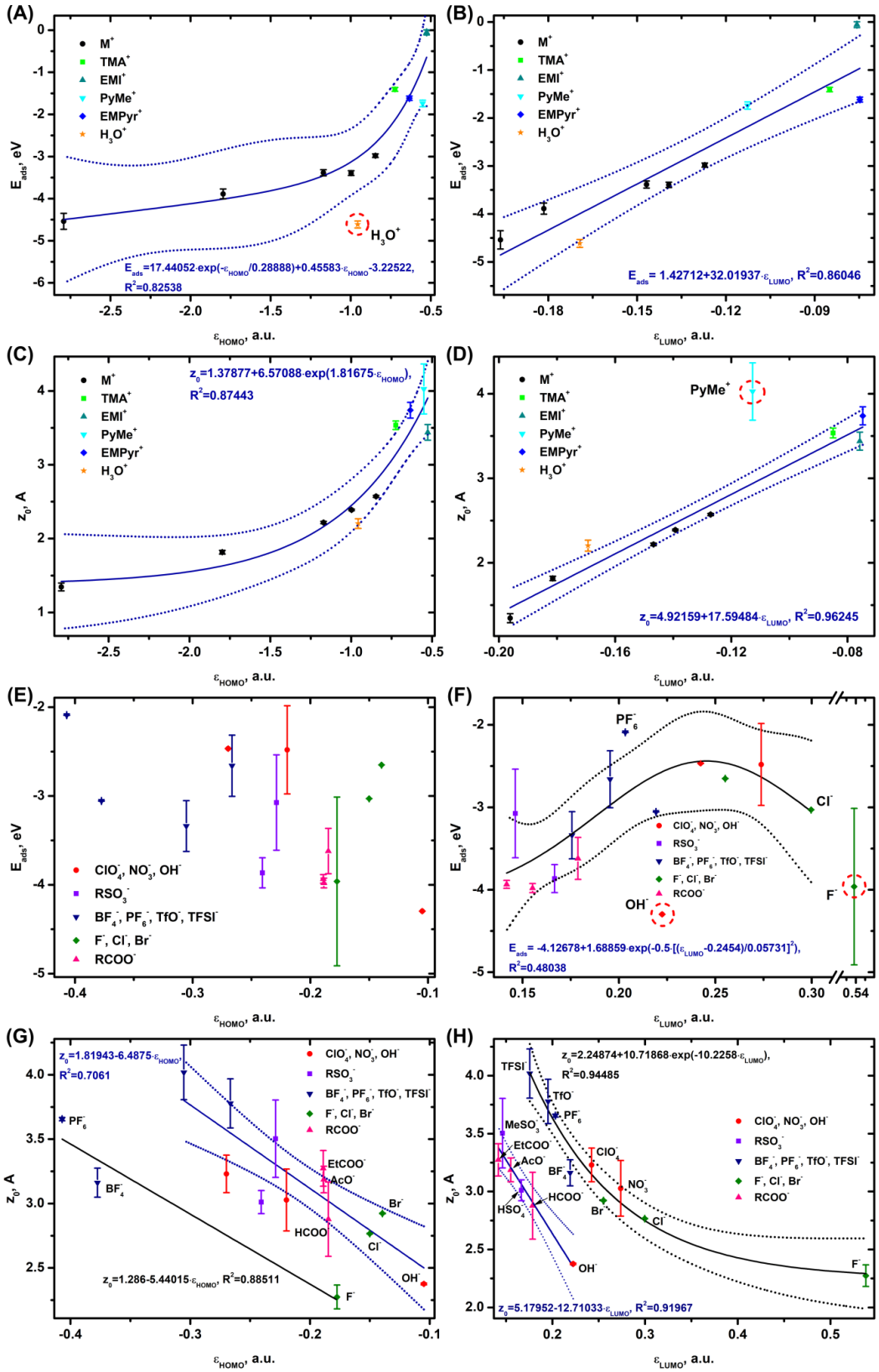

Figure 2. Adsorption energy (**A**, **B**, **E**, **F**) and distance to the surface (**C**, **D**, **G**, **H**) for cations and anions on α-Al_2O_3 (0001) as a function of their HOMO and LUMO orbital energy levels.

Let us continue our consideration of adsorption by studying a semiconductor as an example. As in the previous system, the alkali metal cations are strongly adsorbed on the graphene surface, the $PyMe^+$ cation is weakly bound to the surface. The E_{ads} value for the cations on graphene decreases

 doi:10.20944/preprints202407.1747.v1

linearly as the ε_{HOMO} value becomes lower (**Figure 3 A**) and in case of $E_{ads}(\varepsilon_{LUMO})$, the dependence (**Figure 3 B**) is a volcano-shaped plot with an energy maximum in the region where ε_{LUMO} ~ -0.10 a.u. At the minimum distance from the electrode are the compact alkali metal cations, whereas the farthest from the surface are the voluminous TPA^+ and TBA^+ ions. As the ε_{HOMO} value becomes higher, the z_0 distance from the electrode increases exponentially (**Figure 3 C**), and at an increase in the ε_{LUMO} value, z_0 grows linearly (**Figure 3 D**).

The $E_{ads}(\varepsilon_{HOMO})$ dependence for the anions is almost linear; in case of $E_{ads}(\varepsilon_{LUMO})$ two branches are observed, the first linear one is represented by the ClO_4^-, NO_3^-, OH^-; RSO_3^-; $TFSI^-$, TfO^-, BF_4^-, PF_6^-; and $RCOO^-$ anions and the second one consisting of halides is close to an exponential dependence. Only $i\text{-}PrCOO^-$ is out of the trend. The presence of an i-Pr- voluminous group probably leads to a rather strong repulsion due to the van der Waals interactions, making the adsorption energy value for this ion positive. The lowest adsorption energy values are observed for BF_4^-, PF_6^- and NO_3^-, the highest energies are registered for some of the halides (Cl^-, Br^-), $EtSO_3^-$ and $i\text{-}PrCOO^-$.

$z_0(\varepsilon_{HOMO})$ for the anions splits into two linear dependencies, the first one represented by the BF_4^-, PF_6^-, F^- and OH^- ions, the second one – by the other ions; $i\text{-}PrCOO^-$ and $p\text{-}TsO^-$ are noticeably out of the trend. In case of $p\text{-}TsO^-$, such spread of values may also be caused by the total volume and the associated asymmetry of the system due to the Ph- group, leading to an overestimation of the z_0 distances relative to the trend. The $i\text{-}PrCOO^-$ distance from the electrode is also associated with the voluminous i-Pr group. The $z_0(\varepsilon_{LUMO})$ plot, as the one for the ions on Al_2O_3 (**Figure 2 H**), is formed by a linear dependence consisting of the OH^-; HSO_4^-, $MeSO_3^-$, $EtSO_3^-$, $NH_2SO_3^-$, $p\text{-}TsO^-$; $HCOO^-$, AcO^-, $EtCOO^-$, $PrCOO^-$, and $i\text{-}PrCOO^-$ ions and an exponential dependence consisting of $TFSI^-$, TfO^-, BF_4^-, PF_6^-; ClO_4^-, NO_3^- and halides.

As in case of Al_2O_3, the $E_{ads}(z_0)$ dependence on graphene is observed only for the cations (**Figure S1.13 C**, **D**) and has a volcano shape with a maximum at z_0 ~ 4 Å and E_{ads} ~ -0.5 eV. According to the above dependencies (**Figure 3**) and the data of (**Figure S1.5 B**, **D**), the adsorption of the cations is determined by the HOMO orbital (except HOMO-1), as well as LUMO and LUMO+1. In case of the anions (**Figure 3**, **Figure S1.7 B**, **D**), the HOMO, HOMO-1 and LUMO orbitals are involved in the adsorption.

Preprints.org (www.preprints.org) | NOT PEER-REVIEWED | Posted: 23 July 2024 doi:10.20944/preprints202407.1747.v1

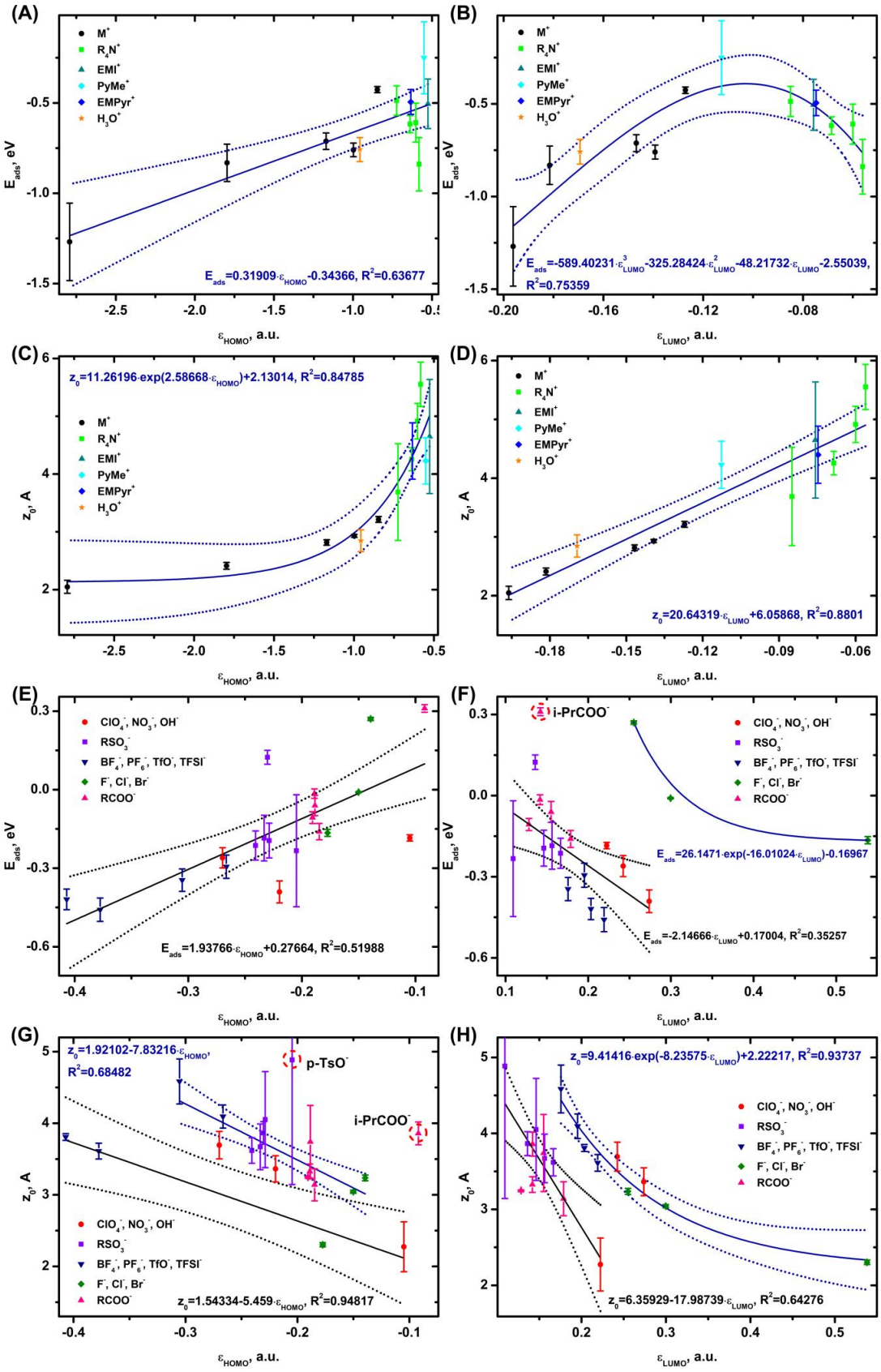

Figure 3. Adsorption energy (**A**, **B**, **E**, **F**) and distance to the surface (**C**, **D**, **G**, **H**) for cations and anions on graphene as a function of their HOMO and LUMO orbital energy levels.

The strongest binding to the gold surface is observed for hydroxonium, which is followed by alkali metal cations and $EMPyr^+$. $PyMe^+$, as in case of graphene, is weakly bound to the surface. For

 doi:10.20944/preprints202407.1747.v1

the Au (111) surface, the voluminous organic $PyMe^+$ and $EMPyr^+$ cations drop out of the exponential dependence of $E_{ads}(\varepsilon_{HOMO})$ and $E_{ads}(\varepsilon_{LUMO})$ (**Figure 4 A**, **B**). In addition, a significant shift towards negative energies is observed for H_3O^+. In case of the alkali metal, TMA^+ and EMI^+ cations, the dependencies are almost exponential, the E_{ads} value in both cases decreases with an increase in ε_{HOMO} and ε_{LUMO}.

z_0 grows exponentially with an increase in ε_{HOMO} and ε_{LUMO} (**Figure 4 C**, **D**). Quite far from the $z_0(\varepsilon_{HOMO})$ dependence are only TMA^+, $EMPyr^+$ and $PyMe^+$. The alkali metal cations, H_3O^+, and EMI^+ fit quite well into the exponential dependence (**Figure 4 C**), and all the ions considered fit into the linear $z_0(\varepsilon_{LUMO})$ dependence (**Figure 4 D**).

Among the anions, the strongest interaction with the surface is observed for halides, which are followed by OH^- and $HCOO^-$. The weakest interaction with the (111) Au surface is observed for the nitrate ion, followed by TfO^- and $MeSO_3^-$. The anions form a characteristic volcano-shaped $E_{ads}(\varepsilon_{HOMO})$ dependence (**Figure 4 E**) with a maximum at ε_{HOMO} ~ -0.25 a.u., while no correlation is found for $E_{ads}(\varepsilon_{LUMO})$ (**Figure 4 F**). The $z_0(\varepsilon_{HOMO})$ dependence is represented by a linear relationship consisting of BF_4^-, PF_6^- and OH^- ions and an exponential relationship with the other systems (**Figure 4 G**). Two dependencies are observed for $z_0(\varepsilon_{LUMO})$ (**Figure 4 H**), with the first linear one formed by OH^-; HSO_4^-, $MeSO_3^-$, $EtSO_3^-$, $NH_2SO_3^-$, p-TsO^-; $HCOO^-$, AcO^-, $EtCOO^-$, $PrCOO^-$, and i-$PrCOO^-$ ions and the second exponential one made up by $TFSI^-$, TfO^-, BF_4^-, PF_6^-; ClO_4^-, NO_3^- and halides.

Some degradation of the correlations on the metal and deviation of a number of cations (on average, cations have stronger binding to Au (111) than anions) can be caused by the increased complexity of the adsorption process of bulk systems on the metal. In addition to a bigger population of electronic states in the metal and, consequently, a bigger number of electrode wave functions involved in the adsorption, there are also local perturbations of the electron density in the vicinity of the ions. In particular, we can talk about image charges, [79,85,86] which can make a significant contribution to the adsorption energy [87] when the adsorbent approaches the metal electrode at a sufficiently close distance. [85]

Unlike the previous model electrodes, on Au (111) the $E_{ads}(z_0)$ dependence is observed for both the cations (an exponential one, **Figure S1.13 E**, except for $PyMe^+$, $EMPyr^+$ and H_3O^+) and the anions (a linear one, **Figure S1.13 F**).

To sum it up (**Figure 4**, **Figure S1.9 B**, **D** and **Figure S1.11 B**, **D**), the adsorption of the cations, except for some systems, and the anions on Au (111) is formed by both HOMO, HOMO-1 and LUMO, LUMO-1. Such conclusion is expectable considering the high density of electronic levels in the metal involved in the adsorption process.

The proposed descriptors characterize the adsorption parameters of cations on Al_2O_3 and graphene quite well (R^2=0.64−0.86 for E_{ads} and R^2=0.87−0.96 for z_0). On Au (111), the correlations for the cations look slightly worse because some organic cations fall out of the dependencies. The correlation coefficients of adsorption and distances for the cations increase as follows: Au (111) < graphene < Al_2O_3 (0001). In case of the anions, the correlations for E_{ads} are somewhat worse R^2=0.35−0.55, but still acceptable for qualitative and semi-quantitative evaluations. And the correlations for the z_0 parameter are approximately at the same level R^2=0.64−0.95 as those for the cations.

Most of the dependencies on the orbital energy are exponential, in some cases they are close to the linear type, as the theoretical estimates suggest (**Figure 1**). Linear dependencies are also reported for the adsorption of neutral molecules on metal oxides in refs. [32–34] Volcano-shaped dependencies are observed for the anions on Al_2O_3 (**Figure 2 F**) and cations on graphene (**Figure 3 B**), which is also in agreement with the theory. The splitting of the dependencies for E_{ads} into two branches is observed only for the anions on graphene (**Figure 3 F**). There is a split in all the z_0 anion dependencies on ε_{HOMO} and ε_{LUMO}. One cause of the division of the anions into two groups may be the presence of several MOs with the same energy (**Table S6.1**). This effect will be discussed in more detail in the next paragraph.

Some limitations on the applicability of ε_{HOMO} and ε_{LUMO} as adsorption descriptors may arise in case of voluminous organic ions whose interaction with the electrode is poorly described by the MO

 doi:10.20944/preprints202407.1747.v1

energy level due to steric perturbations. Another limiting factor may be strong chemisorption involving the formation of a chemical bond with the surface, comparable in energy to the interatomic bond in a solid. In general, the descriptors provided in the manuscript are best suited for characterizing semiconductors and dielectrics.

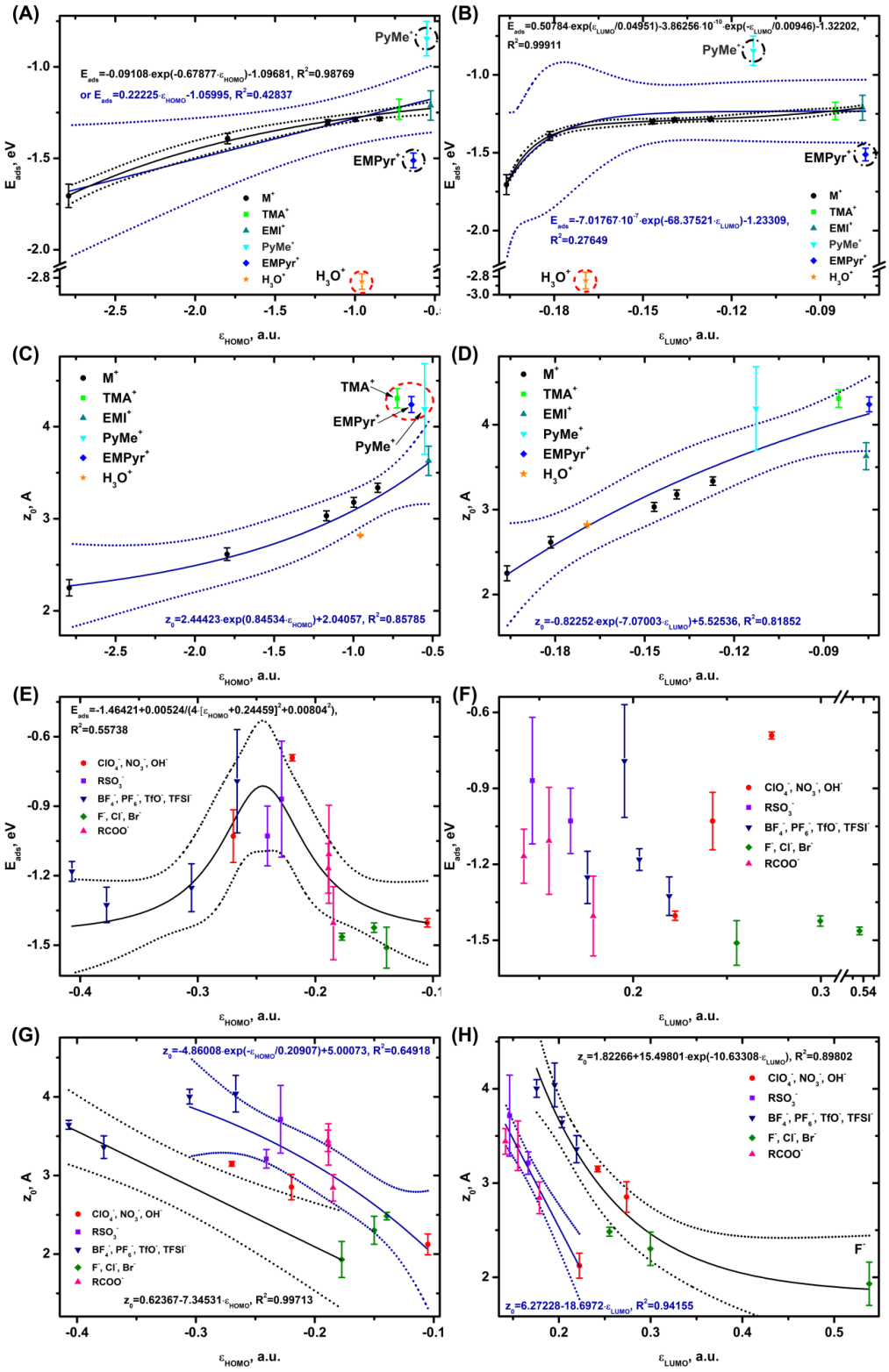

Figure 4. Adsorption energy (**A**, **B**, **E**, **F**) and distance (**C**, **D**, **G**, **H**) to the Au (111) surface for cations and anions as a function of their HOMO and LUMO orbital energy levels. In Figures (**A**) and (**B**), the black colored approximations do not include $PyMe^+$ and $EMPyr^+$, while the royal-colored approximations include these ions.

 doi:10.20944/preprints202407.1747.v1

3.3. Ion Binding in Complexes with Water and Dimethyl Carbonate

The free energy of cation binding into an aqueous complex is described well by an exponential function of ε_{HOMO} (**Figure 5 A**), the TBA^+ cation falls out of the trend, and a polynomial dependence is observed for $G_{bind}(\varepsilon_{LUMO})$ (**Figure 5 B**). The distance from the center of mass of the cation and water is reasonably well described by the exponential $r_0(\varepsilon_{HOMO})$ and linear $r_0(\varepsilon_{LUMO})$ functions (**Figure 5 C**, **D**). Only the pyridinium derivatives (RPy^+) fall out of the $r_0(\varepsilon_{LUMO})$ trend; the distance between the centers of mass for RPy^+ according to quantum chemical calculations is almost 1 Å longer than the obtained trend. The cause of this discrepancy may be greater asymmetry of RPy^+ compared to the other systems. The lowest binding energies and shortest distances are registered for the alkali metal cations, while the highest values are observed for the organic cations.

For the anions, the dependence of G_{bind} on ε_{HOMO} is divided into linear and exponential curves (**Figure 5 E**), while there is no correlation between G_{bind} and ε_{LUMO} (**Figure 5 F**). The lower linear $G_{bind}(\varepsilon_{HOMO})$ correlation (**Figure 5 E**) is formed by BF_4^-, PF_6^-, F^- and OH^- ions, the upper one is made up by ClO_4^-, NO_3^-, DCA^-; $TFSI^-$, TfO^-; Cl^-, Br^-; RSO_3^-; and $RCOO^-$ ions. The ion-water distances (**Figure 5 G**, **H**) depend only on ε_{LUMO}, and no correlations are observed for ε_{HOMO}. The linear dependence of $r_0(\varepsilon_{LUMO})$ is represented by OH^-; HSO_4^-, $MeSO_3^-$, $EtSO_3^-$, $NH_2SO_3^-$, $p\text{-}TsO^-$; $HCOO^-$, AcO^-, $EtCOO^-$, $PrCOO^-$, and $i\text{-}PrCOO^-$ ions, the exponential one – by $TFSI^-$, TfO^-, BF_4^-, PF_6^-; ClO_4^-, NO_3^-; F^-, Cl^-, and Br^- ions. Only DCA^- deviates slightly from the exponential trend. The lowest values of binding energies and distances are observed for F^- and OH^-, while the highest values are observed for the organic cations. The highest values of binding energies are observed for fluorine-containing anions $TFSI^-$, TfO^-, BF_4^-, and PF_6^-, as well as DCA^- and RSO_3^-. The longest r_0 distances are found for BF_4^-, PF_6^- and DCA^-.

For the cations, G_{bind} is exponentially related to r_0 (**Figure S2.9 A**), while for the anions there is no such correlation (**Figure S2.9 B**).

It can be concluded that the HOMO, LUMO (**Figure 5 A**, **B**) and HOMO-1, LUMO+1 orbitals (**Figure S2.1. B**, **D**) are actively involved in the cation binding to water. The anionic aqueous complex is only made up of HOMO and HOMO-1 orbitals (**Figure 5 E**, **Figure S2.3 C**), but not the LUMO orbitals.

 doi:10.20944/preprints202407.1747.v1

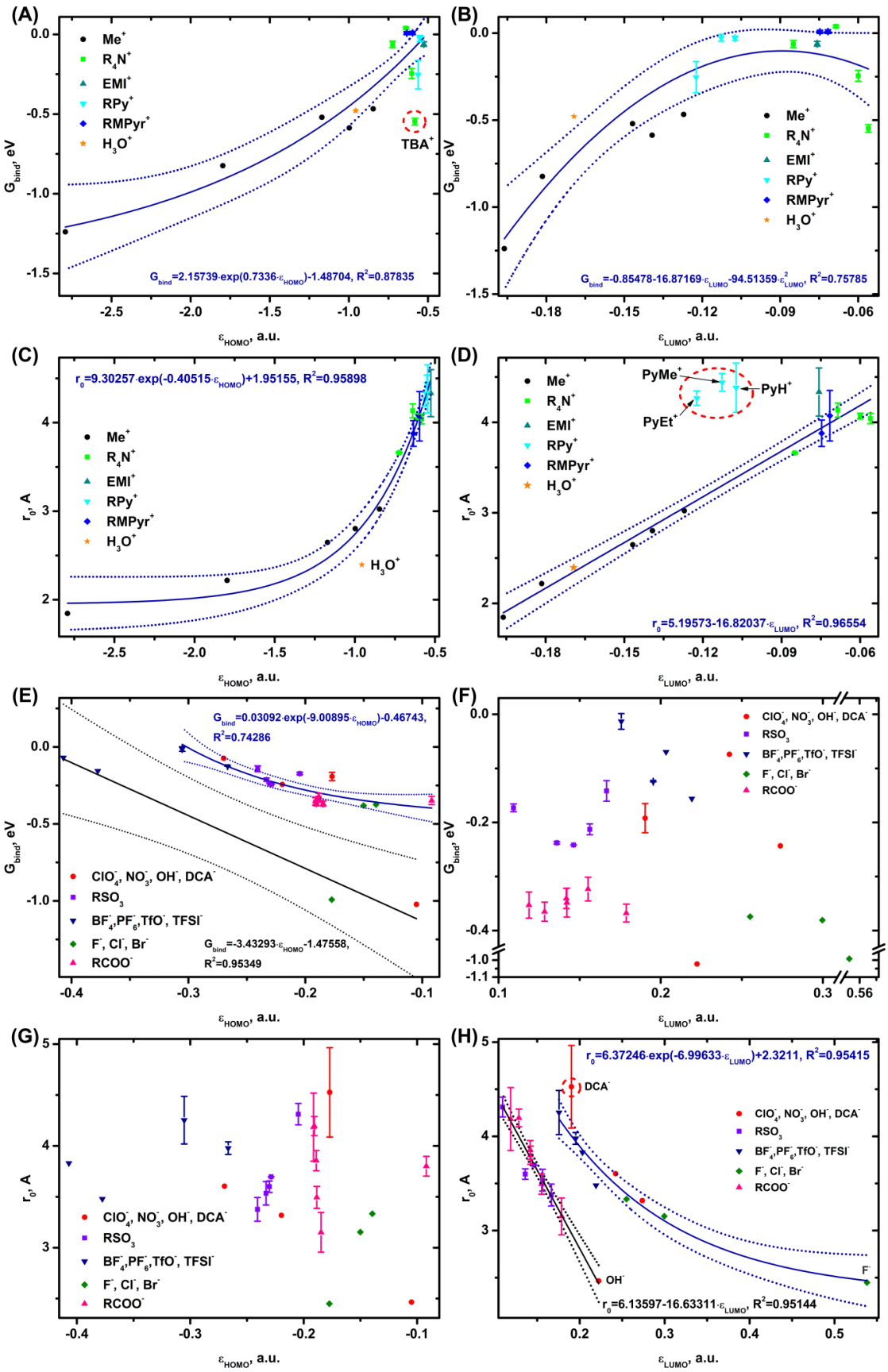

Figure 5. Ion-water binding energies (**A**, **B**, **E**, **F**) and distances (**C**, **D**, **G**, **H**) between the centers of mass of the ions and water molecules as a function of the energy level of the HOMO and LUMO orbitals.

 doi:10.20944/preprints202407.1747.v1

The dependence of the free energy of cation binding to DMC on ε_{HOMO} is approximated by an exponential function (**Figure 6 A**) and on ε_{LUMO} by a polynomial function with a maximum at -0.09 a.u. (**Figure 6 B**). The distances from the center of mass of the cation and DMC grow exponentially depending on ε_{HOMO} and inversely exponentially depending on ε_{LUMO} (**Figure 6 C**, **D**). Only $PyMe^+$ and EMI^+ drop out of the $r_0(\varepsilon_{LUMO})$ dependence, with the predicted r_0 values tending to be almost 1 Å lower than the calculated r_0 ones. The strongest binding to DMC is observed for the alkali metal cations, while the weakest interaction is registered for TEA^+ and $EMPyr^+$.

The plot of the anion binding energy vs ε_{HOMO} represents two linear dependencies (**Figure 6 E**), the first one consisting of PF_6^-, BF_4^- and F^-, the second one — of ClO_4^-, NO_3^-; $MeSO_3^-$; TfO^-, $TFSI^-$, halides and $RCOO^-$ ions. $G_{bind}(\varepsilon_{LUMO})$ is formed (**Figure 6 F**) by a linear relationship composed of $MeSO_3^-$ anions, halides and $RCOO^-$ and an exponential one consisting of ClO_4^-, NO_3^-; PF_6^-, BF_4^-, TfO^-, and $TFSI^-$. Like $G_{bind}(\varepsilon_{HOMO})$, $r_0(\varepsilon_{HOMO})$ for the anions also represents two dependencies (**Figure 6 G**), while $r_0(\varepsilon_{LUMO})$ is a linear relationship (**Figure 6 H**). The strongest interaction with the solvent is observed for F^- and the weakest one — for the $TFSI^-$ and PF_6^- anions.

For the cations, the $G_{bind}(r_0)$ data are approximated by an exponential function (**Figure S2.9 C**) and for the anions — by a linear function (**Figure S2.9 D**).

The HOMO, LUMO (**Figure 6 A**, **B**), HOMO-1, and LUMO+1 orbitals (**Figure S2.6 B**, **D**) are actively involved in the binding of cations to DMC. However, the formation of the anionic complex with DMC involves only the HOMO, LUMO (**Figure 6 E**, **B**), and HOMO-1 (**Figure S2.7 B**) orbitals.

In addition to describing the adsorption on the electrode, the energy level of the HOMO and LUMO is an excellent descriptor of the energy of binding into a complex (R [2]=0.70−0.95) and the distance between the solvent molecule and the ions (R [2]=0.36−0.98). In almost all the cases, the correlation coefficients are much better for the complexes than for the electrodes. Reducing the number of orbitals involved in the binding makes the complex formation easier and closer to theoretical models (paragraph *1*).

The splitting of the dependencies is mainly due to the orbital type of the ion involved in the complex formation. For example, the dependence of the energy of solvent binding to anions on the ε_{HOMO} parameter (**Figure 5 E**, **Figure 6 E**) is split into two curves: one consisting of OH^-, F^-, BF_4^-, and PF_6^- and the second one comprised of the other ions. The MO analysis shows (**Table S6.1**) that the ions from the first dependence possess multiple HOMOs of the same energy. A similar division into two dependencies can be seen in $z_0(\varepsilon_{HOMO})$, for example, for the complexes with DMC (**Figure 6 G**) and for the adsorption of anions on Al_2O_3 (0001) (**Figure 2 G**), graphene (**Figure 3 G**), and Au (111) (**Figure 4 G**). The $z_0(\varepsilon_{LUMO})$ plots are also represented by two dependencies: a linear one consisting of OH^-; RSO_3^-; and $RCOO^-$ and an exponential one composed of ClO_4^-, NO_3^-; BF_4^-, PF_6^-, TfO^-, $TFSI^-$, and halides. There is a similar trend for the adsorption on electrodes (**Figure 2−4 H**) and for complexation with water (**Figure 5 H**), while it is not observed for DMC (**Figure 6 H**). Theoretical evaluations can shed light on the nature of such dependencies by establishing the distance between the ion and the electrode or solvent molecule at which the total energy of the system would be minimized. Taking into account the available data, we can assume that the division is caused by the specific composition of the LUMO orbital and does not depend on the number of LUMO orbitals with the same energy. Taking into account the data on DMC, it is quite natural to conclude that the molecular orbitals of the solvent molecule influence the complex formation.

Preprints.org (www.preprints.org) | NOT PEER-REVIEWED | Posted: 23 July 2024 doi:10.20944/preprints202407.1747.v1

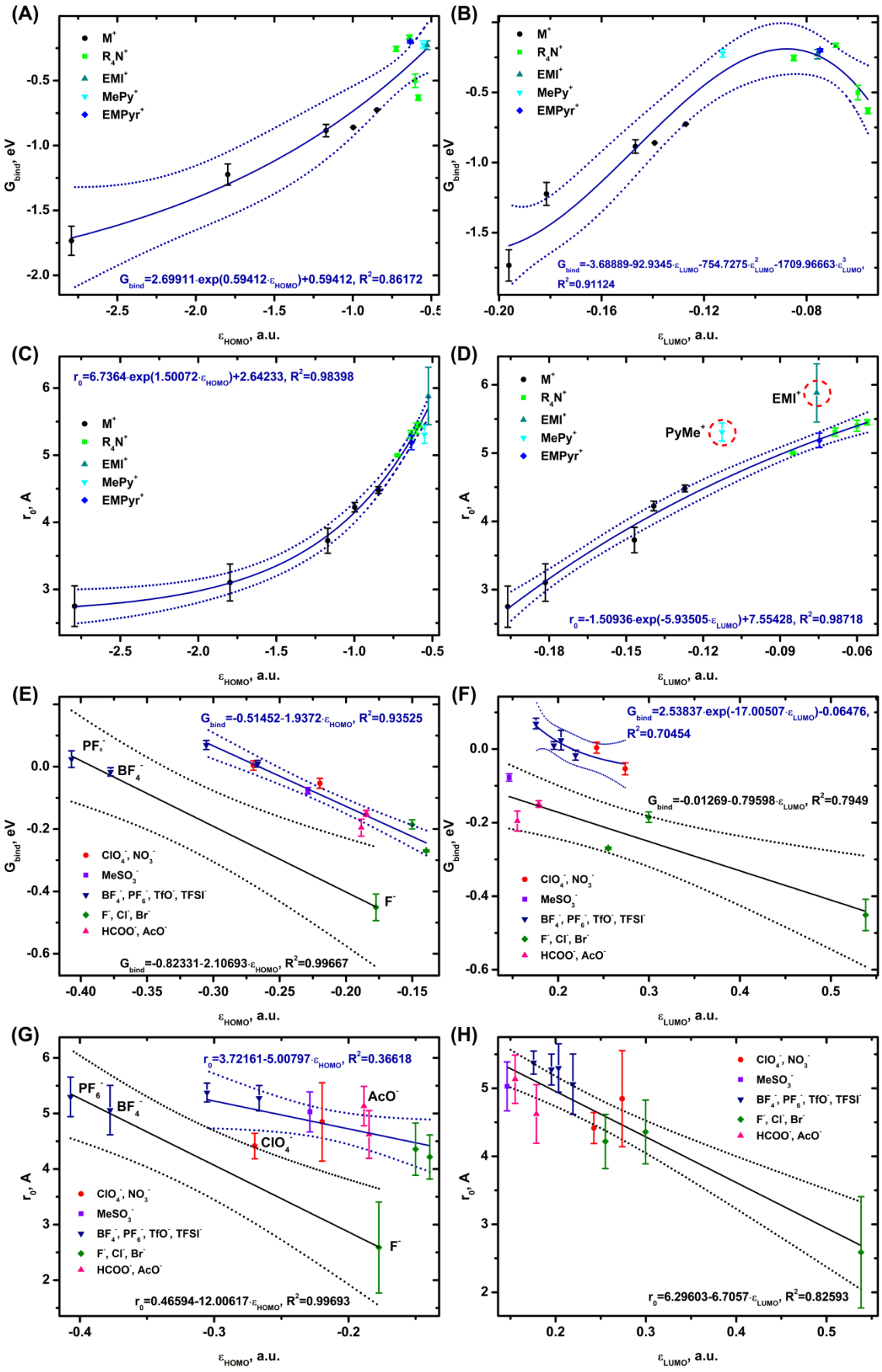

Figure 6. Ion-DMC binding energies (**A**, **B**, **E**, **F**) and distances (**C**, **D**, **G**, **H**) between the centers of mass of the ions and dimethyl carbonate molecules as a function of the energy level of the HOMO and LUMO orbitals.

 doi:10.20944/preprints202407.1747.v1

3.4. Correlations with Physicochemical and Electrochemical Parameters of Ions

Judging by the dependence for dipole moment [88] and the more complicated one for polarization [89] (since the perturbation of the system by the external field is calculated), the wave functions are explicitly included in all the expressions of these parameters. In several models, the wave functions are also included in some terms of the solvation energy expression. [63] Notably, in addition to a number of summands responsible for the environment polarization, [63,64] cavity formation and other contributions, [90] the solvation energy is determined by the first solvation shell, [91,92] which is formed by the solvent directly bound to the ion. As paragraph *3* shows, the energy of binding to water and the intermolecular distances are related to the HOMO and LUMO. The redox potential, in turn, contains the solvation energies of the reactants [93,94] in the original entry and, therefore, depends on the internal rearrangement of the bonds and the environment response to the charge. Such facts and some literature data [35] suggest a possible correlation of the mentioned parameters with the orbital energy level. In general, the mentioned physicochemical parameters, as in works, [26,27] are likely to depend on a whole range of descriptors, but for simplicity of the analysis we will focus on the correlations with MO levels only..

According to the calculations (**Figure 7 A**), the dependence of the dipole moment for the cations on ε_{HOMO} is nearly sigmoidal, for compact one-atom ions (alkali metals) and symmetric ions (TMA^+) in the range ε_{HOMO} = -3 – -0.7 a.u. the dipole moment is equal to zero. Starting from ε_{HOMO} > -0.62 a.u. a sharp increase in the dipole moment value is observed, with the maximum values corresponding to the voluminous and asymmetric CP^+, CTA^+ and DMI^+ cations. The dependence of the dipole moment of anions on ε_{LUMO} (**Figure 7 B**) decreases exponentially in the range ε_{LUMO} = 0.08 − 0.25 a.u., the maximum dipole moment is observed for voluminous DS^-, followed by $BuCOO^-$, $p\text{-}TsO^-$. At ε_{LUMO} > 0.25 a.u. the dipole moment of the anions becomes close to zero (for halides and symmetric NO_3^-, ClO_4^-, etc.).

The polarization dependence on ε_{HOMO} for the cations (**Figure 7 C**) is split into two curves: an exponential one represented by H_3O^+, alkali metal cations, $RMPyr^+$, and R_4N^+, and a linear one represented by CTA^+, CP^+, RMI^+ (except $PhMI^+$, which is out of the trend), and RPy^+. The dependence of P on ε_{LUMO}, as the one for the dipole moment, decreases exponentially (**Figure 7 D**), with $TFSI^-$ falling out of the trend. The maximum polarization values are obtained for the voluminous and heavy DS^- and $p\text{-}TsO^-$ cations, the lowest ones for the light F^-, OH^- and BF_4^- ions.

The value of the solvation energy for the cations decreases exponentially with an increase in the ε_{HOMO} or ε_{LUMO} values (**Figure 7 E**, **F**). The lowest solvation values are observed for Li^+, which is followed by the other alkali metals, with the maximum values obtained for the organic cations. The $G_{solv}(\varepsilon_{HOMO-1})$ dependence for the anions has a characteristic volcano shape with a maximum at ε_{HOMO-1} = -0.42 a.u. (**Figure 7 G**). The left part of the dependence is formed by the halides, the right part – by the other ions. A significant deviation from the trend is observed for OH^-, the energy value of which is significantly underestimated. $TFSI^-$, the solvation energy of which is slightly overestimated, is out of the trend. The lowest values of G_{solv} are observed for F^-, OH^- and the highest values for $TFSI^-$.

A dependence of the oxidation potentials on ε_{HOMO} is only observed for the anions (**Figure 7 H**). E_{SHE} decreases exponentially as ε_{HOMO} goes up.

The present paragraph clearly shows that in addition to describing the adsorption of ions or their binding to the solvent, the HOMO and LUMO parameters are also well suited for characterizing a number of physicochemical and electrochemical parameters. The latter, first of all, include dipole moment and polarization, whose correlation coefficients of the approximations reach R^2=0.8−0.94 and the cation solvation energy R^2=0.95. Slightly worse are R^2=0.74−0.78, but there are clear dependencies on the solvation energy and oxidation potential of anions.

 doi:10.20944/preprints202407.1747.v1

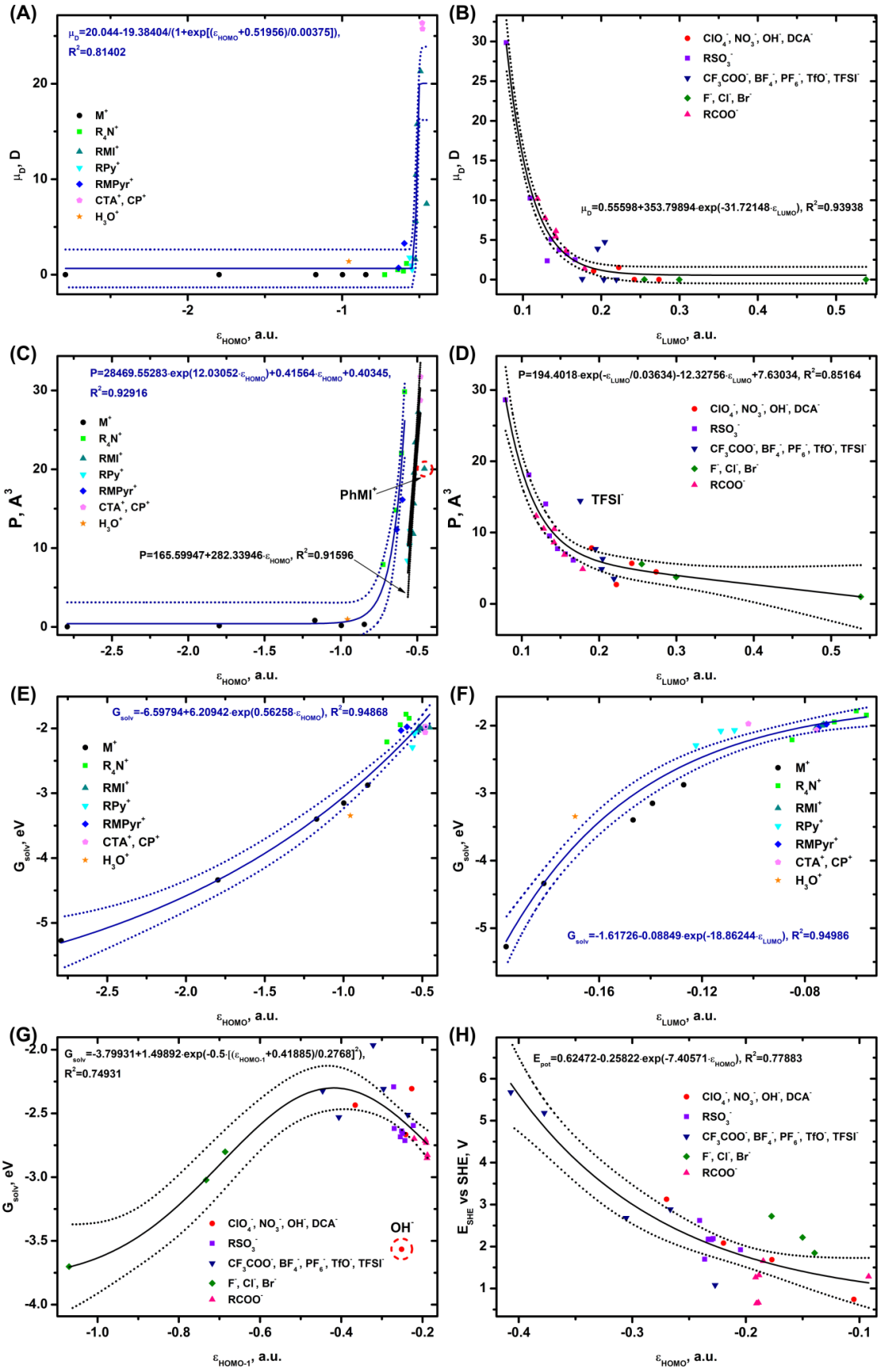

Figure 7. Dependence of the dipole moment (**A**, **B**), polarizability (**C**, **D**), solvation energy (**E**–**G**) and oxidation potential (**H**) of ions on their HOMO, HOMO-1 and LUMO orbital levels.

 doi:10.20944/preprints202407.1747.v1

3.5. Practical Evaluations

In this paragraph, we will show how orbital values can be applied to solving a practical problem. For this purpose, in continuation of the study of aqueous electrolytes, [28,44–47,50,51] let us consider the ability of cations and anions to displace water from the inner layer of the electric double layer (EDL). The point of this task is to displace the electroactive component of the electrolyte water as far away from the electrode surface as possible [28,44–46] and, as a result, to increase the electrochemical potential window and energy capacity of the batteries. Since such problem considers a potential electrolyte for a battery, we will use a Li^+ ion as the cation. The parameters of the anions will be calculated using the approximations obtained previously (**Table S2.3**, **S3.3**, **S5.3**). We will use graphene as the electrode because it can serve as a simplified model system representing different carbon materials for supercapacitors [95,96] and batteries. [97,98] By varying the ε_{HOMO} and ε_{LUMO} parameters in the range characteristic of anions, we will find systems with the minimal water concentration in the inner layer of EDL.

Under equilibrium conditions, the reversible process of displacement of ions (i) by water molecules (w) in the inner layer from the surface into the bulk $i^{bulk} + w^{surf} \rightleftarrows i^{surf} + n_i w^{bulk}$ is described by a multicomponent adsorption isotherm: [99–101]

$$\ln\frac{\theta_i}{\theta_w^{n_i}} + \ln\frac{f_i^{surf}}{\left(f_w^{surf}\right)^{n_i}} = \ln\left\{\beta_i\frac{f_i^{bulk}c_i^{bulk}}{\left(f_w^{bulk}c_w^{bulk}\right)^{n_i}}\right\} - \frac{q_i e_0 \varphi_d}{k_B T} - \left\{\frac{q_i e_0 \left(l_{eff} - r_i\right)}{l k_B T} + b_i - n_i b_w\right\}\Delta\varphi + \left(c_i - n_i c_w\right)\Delta\varphi^2 \quad (\mathbf{10}),$$

and parameters

$$b_j = \mu_j / l_{eff} k_B T \ (j = i, w) \quad (\mathbf{11}),$$

$$c_j = \varepsilon_0 \varepsilon_j A_j / 2 l_{eff} k_B T \quad (\mathbf{12}),$$

where θ_i and θ_w are the degrees of surface coverage by ions and water molecules, $\Delta\varphi = \frac{\left(\sigma_0 + \sigma_{ions}\right) l_{eff}}{\varepsilon_{eff}\varepsilon_0}$ is the potential drop in the inner layer of the EDL, σ_0 is the surface charge density on the electrode, $\sigma_{ions} = \sum_i \frac{\theta_i q_i e_0}{\pi r_i^2}$ is the surface charge density of adsorbed ions in the inner layer, $\varphi_d = \frac{2RT}{F}\operatorname{arcsin h}\left(\frac{-(\sigma_0 + \sigma_{ions})}{\sqrt{8RT\varepsilon_b\varepsilon_0 c_0 \cdot 1000}}\right)$ is the potential drop in the diffuse layer according to the Gui-Chapman model, [102] ε_b is the dielectric permittivity of the solution in the bulk (since dilute aqueous solutions are considered, the value is approximated as 78 [103]), c_0 is the concentration of the supporting electrolyte in mol/L, q_i is the i ion charge, $n_i = r_i^2 / r_w^2$ is the ratio of areas of the i ion and water molecule, r_i and r_w are the effective radius of the ion or water molecule. [28]

The parameters included in coefficients b_j and c_j (**11**,**12**) have the following physical meaning: μ_j is the dipole moment perpendicular to the electrode surface; $\varepsilon_j = 1 + P_j / \varepsilon_0 A_j l_{eff}$ is the dielectric constant of component j, calculated according to the model described in ref. [104] (P_j is the polarizability); $A_j = 2\pi r_j^2$ is the area occupied by component j; $\varepsilon = \sum_{j=i,w} \varepsilon_j \theta_j$ and $l_{eff} = \sum_{j=i,w} z_j \theta_j$ are the effective values of the dielectric constant and thickness of the inner layer.

The $f_i^{surf} / \left(f_w^{surf}\right)^{n_i}$ ratio of the activity coefficients of the electrolyte components in the inner layer according to the mean field approximation [99,100] is generally determined by the expression

 doi:10.20944/preprints202407.1747.v1

$$\ln\frac{\theta_m}{f_W^{r_m}} = \left\{\theta_w(1-\theta_m) - r_m\theta_m(1-\theta_w)\right\}A_{mk+1} + \sum_{g\neq m,k+1}\theta_g(1-\theta_m+r_m\theta_m)A_{gm} - \sum_{g\neq m,k+1}\left\{\theta_w\theta_g + r_m\theta_g(1-\theta_w)\right\}A_{gk+1} + \sum_{g<h}\theta_g\theta_h(r_m-1)A_{gh} \quad (13)$$

For a 1:1 electrolyte (A stands for cations, B designates anions) and a solvent, equation (**13**) looks as follows:

$$\ln\frac{f_A}{f_W^{n_A}} = \theta_B\left\{1+(n_A-1)\theta_A\right\}A^{AB} + \left\{\theta_W(1-\theta_A) - \theta_A(1-\theta_W)n_A\right\}A^{AW} - \theta_B\left\{n_A-(n_A-1)\theta_W\right\}A^{BW} \quad (14)$$

$$\ln\frac{f_B}{f_W^{n_B}} = \theta_A\left\{1+(n_B-1)\theta_B\right\}A^{AB} + \left\{\theta_W(1-\theta_B) - \theta_B(1-\theta_W)n_B\right\}A^{BW} - \theta_A\left\{n_B-(n_B-1)\theta_W\right\}A^{AW} \quad (15)$$

If k≠m, the A_{km} coefficients between components k and m are written as

$$A_{km} = z_{CN}\left\{E_{km} - (E_{kk}+E_{mm})/2\right\}/k_BT \quad (16)$$

where z_{CN} is the effective coordination number in the two-dimensional lattice, E is the energy of the interaction between the electrolyte components, when k=i and m=w: E_{iw} is the energy of binding of the ion and the water molecule (taken equal to the free binding energy of the components in the following estimations), E_{ww} is the energy of binding of the water molecules into a dimer, E_{ii} is the energy of binding of the ions with each other.

For simplicity, E_{ii} is represented as a Coulomb interaction of charges q_i separated from each other by the distance of their own effective ionic radii: $E_{AA} = \frac{1}{4\pi\varepsilon_0\varepsilon_{eff}}\frac{q_+^2e_0^2}{(2r_+)}$ for two cations, $E_{BB} = \frac{1}{4\pi\varepsilon_0\varepsilon_{eff}}\frac{q_-^2e_0^2}{(2r_-)}$ for two anions, and $E_{AB} = \frac{1}{4\pi\varepsilon_0\varepsilon_{eff}}\frac{q_+q_-e_0^2}{(r_++r_-)}$ for one cation and one anion.

β_i is the parameter which determines the difference between the chemical potentials of the reaction components on the surface and in the bulk.

$$\ln(\beta_i) = \left\{\left(\mu_i^{0,bulk} - \mu_i^{0,surf}\right) - n_i\left(\mu_w^{0,bulk} - \mu_w^{0,surf}\right)\right\}/k_BT \quad (17)$$

To simplify the problem, let us write this parameter as a function of the adsorption energies of the components on the electrode

$$\ln(\beta_i) = \left\{(-E_{i,ads}) - n_i(-E_{w,ads})\right\}/k_BT = \left(n_iE_{w,ads} - E_{i,ads}\right)/k_BT \quad (18)$$

As work [28] suggests, the effective radius of cations should be estimated taking into account the solvation water. Keeping that in mind, we used the following parameters as the initial data for the lithium cation with a correction for solvation water: E_{ads} = -1.27 eV, $E_{bind,w}$ = -0.33 eV, r_{Li^+} = 3.00 Å (including the solvation water (**Table S7.1**)), z_0 = 3.45 Å, μ and P are equal to zero; the parameters for the water molecule are E_{ads} = -0.11 eV, r_w = 1.41 Å, z_0 = 3.29 Å, μ = 2.19 D, P =7.21 Å [3], E_{ww} = -0.13 eV. We described the dipole moment and polarizability of all the anions by the expressions μ_D=0.55598+353.79894·exp(-31.72148·ε_{LUMO}) and P=194.4018·exp(-ε_{LUMO}/0.03634) 12.32756·ε_{LUMO}+7.63034. The effective coordination number was taken to be z_{CN} = 6.

In accordance with the specific features of the dependencies of adsorption of the anions and their interaction with water on ε_{HOMO} and ε_{LUMO}, we divided all the systems into three sets (**Figure 8 A**, **B**, **C**).

Preprints.org (www.preprints.org) | NOT PEER-REVIEWED | Posted: 23 July 2024 doi:10.20944/preprints202407.1747.v1

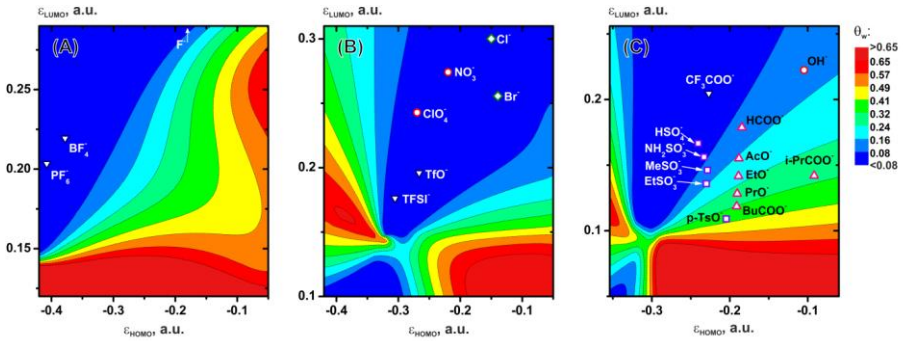

Figure 8. Water coverage (θ_w) of the model electrode depending on the value of the anion ε_{HOMO} and ε_{LUMO}, Li^+ is used as the cation, the concentration of the supporting electrolyte is 1 M. (**A**) – F^-, BF_4^- and PF_6^-, (**B**) – $TFSI^-$, TfO^-, ClO_4^-, NO_3^- and Cl^-, Br^-, (**C**) – OH^-, HSO_4^-, CF_3COO^-, RSO_3^-, and $RCOO^-$ anions.

The first set of systems (**A**) consists of F^-, BF_4^- and PF_6^-; the adsorption of these ions is described by the expressions: E_{ads}=1.93766·ε_{HOMO}+0.27664 and z_0=1.54334-5.459·ε_{HOMO}, the aqueous complex parameters – by the expressions G_{bind}=-3.43293·ε_{HOMO}-1.47558 and r_0=6.13597-16.63311·ε_{LUMO}. According to the obtained solutions (**Figure 8 A**) to equations (**10–18**), the lowest water coverage degree (θ_w < 0.08) is observed for the BF_4^- and PF_6^- ions. The only practical limitation on using BF_4^- and PF_6^- as aqueous electrolytes is their slow hydrolysis, [105–109] which is why they have not been mentioned as salts for aqueous systems. **Figure 8 A** does not show F^-, which lies much higher at ε_{LUMO}= 0.54 a.u., but this system also extends to the region of low values θ_w < 0.08. In contrast to BF_4^- and PF_6^-, the fluoride appears in studies [97,110] as a component of an aqueous electrolyte with a wide potential window.

The second set of systems (**B**) is represented by ions whose adsorption is described in a way similar to the systems in (**Figure 8 A**), except for the parameter z_0=1.92102-7.83216·ε_{HOMO}, and the aqueous complex parameters are expressed as G_{bind}=0.03092·exp(-9.00895·ε_{HOMO})-0.46743 and r_0=6.13597-16.63311·ε_{LUMO}. All the systems (**Figure 8 B**) lie in the region θ_w < 0.08. Almost all of the above systems are reported in the literature as aqueous electrolytes with a wide potential window: $TFSI^-$, [44–46] TfO^-, [111] ClO_4^-, [112,113] and NO_3^-. [114,115] The exceptions are Cl^- and Br^- halides, whose electroactivity is quite high, especially that of Br^-, due to the relatively low oxidation potential, which limits their use in high voltage electrolytes. Only KCl is employed in supercapacitors but its use is limited too. [116–118]

The third set of systems (**C**) is represented by OH^-, HSO_4^-, CF_3COO^-, RSO_3^-, and $RCOO^-$ anions whose adsorption is described by expressions similar to those in (**Figure 8 B**), the parameters of interaction with water are described by the equations G_{bind}=0.03092·exp(-9.00895·ε_{HOMO})-0.46743 and r_0=6.37246·exp(-6.99633·ε_{LUMO})+2.3211. The lowest water coverage θ_w < 0.08 (**Figure 8 C**) is observed for the CF_3COO^- system as well as for HSO_4^- and $NH_2SO_3^-$. CF_3COO^- is mentioned in refs. [119,120] In general, the application of such system is limited by their cost and toxicity. HSO_4^- in an aqueous medium is characterized by dissociation with a marked pH decrease, [121] which significantly narrows the potential window by shifting the cathodic region in the acidic medium. $NH_2SO_3^-$ is electrochemically unstable as the experiments and calculations show. [28] The $MeSO_3^-$, $EtSO_3^-$, and $HCOO^-$ systems lie in the moderate water coverage degree region 0.08 < θ_w < 0.16, AcO^- lies at the boundary of the region θ_w ~ 0.16. OH^- itself is quite electroactive and shifts the potential window; however, in concentrated alkalis the potential window slightly increases to ~1.6 V, [116,117,122,123] which is higher than in pure water (1.23 V [115]). Such systems are used in supercapacitors. [116,117,123] In practice, sulfonate is more often used in its acid form as an additive to electrolytes in electroplating and hydrometallurgy, [124] and as an anion in redox flow batteries. [125] $EtSO_3^-$ has hardly ever been mentioned as an aqueous electrolyte in the literature, except for some references where it was mentioned as an electrolyte for zinc-ion batteries. [126] $HCOO^-$ as an electrolyte was mentioned in ref. [127]; in general, alkaline salts of carboxylic acids are often reported as potential electrolytes. [28,127–130]

 doi:10.20944/preprints202407.1747.v1

The low values of the electrode water coverage in electrolytes are in most cases consistent with the electrochemical stability of the system, confirming that the coverage is one of the main parameters [28] determining the potential window. In addition to the known systems, electrolytes with anions represented by sulfonic acid derivatives are potentially interesting as objects of further investigation. Of course, a comprehensive analysis of the ion suitability for electrolytes requires, in addition to the water coverage, evaluation of the electrochemical stability of the anion itself and its potential intermediates during electrochemical decomposition, as it was done in case of $NH_2SO_3^-$. [28]

The use of the ε_{HOMO} and ε_{LUMO} parameters makes it possible to quickly evaluate the water coverage of the electrode and select the optimal anions, as it has been shown by a particular example. Due to the dependencies of the other electrochemical parameters (solvation energy, redox potential, etc.) on MO energy levels, such analysis can be performed in a comprehensive way, taking into account all the necessary parameters of cations and anions at the same time.

4. Conclusions

In contrast to a lot of other works that study the effect of the electrode material or solvent type on the interactions of ions with the electrode surface and solvent molecules, the present work shows the dependence of these interactions on the ion nature. The calculations carried out using theoretical models of adsorption and complex formation for ions showed that the energy of adsorption on the electrode or the energy of binding into a complex with the solvent depends on the energy of the ion valence orbital. Most of the obtained dependencies are close to linear and exponential types, in some cases the solution leads to volcano-shaped dependencies.

A comparison of a number of ion parameters obtained by quantum chemical calculations revealed clear correlations with the HOMO and LUMO energies of the ion orbitals. The first parameter to be considered was the adsorption energies on model electrodes represented by aluminum oxide (0001), graphene and Au (111). The best correlations were observed for graphene and aluminum oxide; in case of gold, some deviations were found for the organic cations. Volcano-like correlations were revealed between the adsorption energy of anions on Al_2O_3 (0001) and graphene surfaces with ε_{LUMO}, and on Au (111) with ε_{HOMO}. Strong correlations were found for the energies of ion binding to solvent molecules represented by water and dimethyl carbonate. Volcano-like dependencies were also observed for the energy of binding of cations to H_2O and DMC on ε_{LUMO}. In addition, a clear relationship was observed between the dipole moment, polarization and solvation energy of ions, on the one hand, and the HOMO and LUMO energy level. For the anions, the oxidation potential was found to be dependent on the HOMO energy level.

The described dependencies of the ion parameters on the energy levels of molecular orbitals were approximated by expressions that allow us to use the energy level of orbitals as a descriptor in applied problems. The use of such parameters makes the search for ions with desired properties a lot easier. First of all, such descriptors can be relevant in the field of catalysis, especially for catalyst surface composition control and in surface chemistry, for example, when searching for ions with the highest adsorption for a given material to solve the problem of heavy metal binding by different sorbents. An example of possible practical application of the descriptors was clearly demonstrated by aqueous electrolytes for batteries. Li^+ was used as the cation, the anion parameters were estimated by the previously obtained expressions, the task was to select an anion the use of which would minimize the degree of water coverage of the electrode surface. Reduction in the water coverage increases the working window potential of the electrolyte. The obtained estimates for the anions widely applied in electrochemical practice agree with the experimental data, new electrolytes can be potentially found among alkaline salts of sulfonic acid derivatives.

Supplementary Materials: The following supporting information can be downloaded at the website of this paper posted on Preprints.org.

Acknowledgments: Calculations were made using resources of the Joint Supercomputer Center of the Russian Academy of Sciences.

 doi:10.20944/preprints202407.1747.v1

Conflicts of interest: There are no conflicts to declare.

References

1. B. Li, W. Gao and Q. Jiang, Electronic and Geometric Determinants of Adsorption: Fundamentals and Applications. *Journal of Physics: Energy* **2021**, *3* (2), 022001. https://doi.org/10.1088/2515-7655/abd295.
2. Z.-J. Zhao, S. Liu, S. Zha, D. Cheng, F. Studt, G. Henkelman and J. Gong, Theory-Guided Design of Catalytic Materials Using Scaling Relationships and Reactivity Descriptors. *Nature Reviews Materials* **2019**, *4* (12), 792–804. https://doi.org/10.1038/s41578-019-0152-x.
3. D. M. Newns, Self-Consistent Model of Hydrogen Chemisorption. *Physical Review* **1969**, *178* (3), 1123–1135. https://doi.org/10.1103/physrev.178.1123.
4. B. Hammer, J.K. Nørskov, (1997). Theory of Adsorption and Surface Reactions. In: Lambert, R.M., Pacchioni, G. (eds) Chemisorption and Reactivity on Supported Clusters and Thin Films. NATO ASI Series, vol 331. Springer, Dordrecht. https://doi.org/10.1007/978-94-015-8911-6_11
5. B. Hammer, Special Sites at Noble and Late Transition Metal Catalysts. *Top Catal*, **2006**, *37*, 3–16. https://doi.org/10.1007/s11244-006-0004-y
6. J. Suntivich, H. A. Gasteiger, N. Yabuuchi, H. Nakanishi, J. B. Goodenough and Y. Shao-Horn, Design Principles for Oxygen-Reduction Activity on Perovskite Oxide Catalysts for Fuel Cells and Metal–Air Batteries. *Nature Chemistry* **2011**, *3* (7), 546–550. https://doi.org/10.1038/nchem.1069.
7. M. M. Jaksic and J. M. Jaksic Fermi Dynamics and Some Structural Bonding Aspects of Electrocatalysis for Hydrogen Evolution. *Electrochimica Acta* **1994**, *39* (11–12), 1695–1714. https://doi.org/10.1016/0013-4686(94)85155-7.
8. J. M. Jakšić, N. V. Krstajić, B. N. Grgur and M. M. Jakšić, Hydridic and Electrocatalytic Properties of Hypo-Hyper-d-Electronic Combinations of Transition Metal Intermetallic Phases*1. *International Journal of Hydrogen Energy* **1998**, *23* (8), 667–681. https://doi.org/10.1016/s0360-3199(97)00091-8.
9. F. Abild-Pedersen, J. Greeley, F. Studt, J. Rossmeisl, T.R. Munter, P.G. Moses, E. Skúlason, T. Bligaard and J.K. Nørskov, Scaling Properties of Adsorption Energies for Hydrogen-Containing Molecules on Transition-Metal Surfaces. *Physical Review Letters* **2007**, *99* (1). https://doi.org/10.1103/physrevlett.99.016105.
10. F. Calle-Vallejo, N. G. Inoglu, H.-Y. Su, J. I. Martínez, I. C. Man, M. T. M. Koper , J. R. Kitchin and J. Rossmeisl Number of Outer Electrons as Descriptor for Adsorption Processes on Transition Metals and Their Oxides. *Chemical Science* **2013**, *4* (3), 1245. https://doi.org/10.1039/c2sc21601a.
11. W. Gao, Y. Chen, B. Li, S.-P. Liu, X. Liu and Q. Jiang Determining the Adsorption Energies of Small Molecules with the Intrinsic Properties of Adsorbates and Substrates. *Nature Communications* **2020**, *11* (1). https://doi.org/10.1038/s41467-020-14969-8.
12. S.V. Doronin, N.V. Dokhlikova and M.V. Grishin. Descriptor of Catalytic Activity Nanoparticles Surface: Atomic and Molecular Hydrogen on Gold. *Molecular Catalysis* **2022**, *529*, 112534. https://doi.org/10.1016/j.mcat.2022.112534.
13. Y. Jiao, Y. Zheng, K. Davey and S.-Z. Qiao. Activity Origin and Catalyst Design Principles for Electrocatalytic Hydrogen Evolution on Heteroatom-Doped Graphene. *Nature Energy* **2016**, *1* (10). https://doi.org/10.1038/nenergy.2016.130.
14. S. V. Doronin, A. A. Volykhov, A. I. Inozemtseva, D. Yu. Usachov and L. V. Yashina, Comparative Catalytic Activity of Graphene Imperfections in Oxygen Reduction Reaction. *The Journal of Physical Chemistry C* **2020**, *124* (11), 6038–6053. https://doi.org/10.1021/acs.jpcc.9b09668.
15. A. Kulkarni, S. Siahrostami, A. Patel and J. K. Nørskov, Understanding Catalytic Activity Trends in the Oxygen Reduction Reaction. *Chemical Reviews* **2018**, *118* (5), 2302–2312.

https://doi.org/10.1021/acs.chemrev.7b00488.

16. B. Jiang, Y. Tian, Y. An, R. Liu and F. Shaik, Electrocatalytic Activity Analysis of Vinegar Residue-Based Heteroatom-Doped Carbon Quantum Dots Integrated on Vertically Aligned Graphene Arrays for Hydrogen Evolution Reaction. *International Journal of Hydrogen Energy* **2023**, *48* (98), 38686–38698. https://doi.org/10.1016/j.ijhydene.2023.06.092.
17. X. Cui, C. Tang and Q. Zhang. A Review of Electrocatalytic Reduction of Dinitrogen to Ammonia under Ambient Conditions. *Advanced Energy Materials* **2018**, *8* (22). https://doi.org/10.1002/aenm.201800369.
18. R. Manjunatha, A. Karajić, M. Liu, Z. Zhai, L. Dong, W. Yan, D. P. Wilkinson and J. Zhang, A Review of Composite/Hybrid Electrocatalysts and Photocatalysts for Nitrogen Reduction Reactions: Advanced Materials, Mechanisms, Challenges and Perspectives. *Electrochemical Energy Reviews* **2020**, *3* (3), 506–540. https://doi.org/10.1007/s41918-020-00069-0.
19. Z. Masoumi, M. Tayebi, M. Tayebi, S. A. Masoumi Lari, N. Sewwandi, B. Seo, C.-S. Lim, H.-G. Kim and D. Kyung, Electrocatalytic Reactions for Converting CO2 to Value-Added Products: Recent Progress and Emerging Trends. *International Journal of Molecular Sciences* **2023**, *24* (12), 9952. https://doi.org/10.3390/ijms24129952.
20. M.S. Sajna, S. Zavahir, A. Popelka, P. Kasak, A. Al-Sharshani, U. Onwusogh, M. Wang, H. Park and D. S. Han, Electrochemical System Design for CO2 Conversion: A Comprehensive Review. *Journal of Environmental Chemical Engineering* **2023**, *11* (5), 110467. https://doi.org/10.1016/j.jece.2023.110467.
21. C. Cardenas, N. Rabi, P. W. Ayers, C. Morell, P. Jaramillo and P. Fuentealba. Chemical Reactivity Descriptors for Ambiphilic Reagents: Dual Descriptor, Local Hypersoftness, and Electrostatic Potential. *The Journal of Physical Chemistry A* **2009**, *113* (30), 8660–8667. https://doi.org/10.1021/jp902792n.
22. R.G. Pearson, The Electronic Chemical Potential and Chemical Hardness. *Journal of Molecular Structure: THEOCHEM* **1992**, *255*, 261–270. https://doi.org/10.1016/0166-1280(92)85014-c.
23. V. K. Choudhary, A. K. Bhatt, D. Dash and N. Sharma, DFT Calculations on Molecular Structures, HOMO–LUMO Study, Reactivity Descriptors and Spectral Analyses of Newly Synthesized Diorganotin(IV) 2-chloridophenylacetohydroxamate Complexes. *Journal of Computational Chemistry* **2019**, *40* (27), 2354–2363. https://doi.org/10.1002/jcc.26012.
24. M. Karelson, V.S. Lobanov and A.R. Katritzky, Quantum-Chemical Descriptors in QSAR/QSPR Studies. *Chemical Reviews* **1996**, *96* (3), 1027–1044. https://doi.org/10.1021/cr950202r.
25. A. Kokalj, On the Alleged Importance of the Molecular Electron-Donating Ability and the HOMO–LUMO Gap in Corrosion Inhibition Studies. *Corrosion Science* **2021**, *180*, 109016. https://doi.org/10.1016/j.corsci.2020.109016.
26. M. H. Abraham and W. E. Acree, The Transfer of Neutral Molecules, Ions and Ionic Species from Water to Wet Octanol. *Physical Chemistry Chemical Physics* **2010**, *12* (40), 13182. https://doi.org/10.1039/c0cp00695e.
27. M. H. Abraham, W. E. Acree, Descriptors for Ions and Ion-Pairs for Use in Linear Free Energy Relationships. *Journal of Chromatography A* **2016**, *1430*, 2–14. https://doi.org/10.1016/j.chroma.2015.07.023.
28. S. V. Doronin and M. A. Nazarov, Superconcentrated Electrolytes for Aqueous Batteries Based on Alkali Metal Formates and Propionates. *The Journal of Physical Chemistry C* **2022**, *126* (34), 14611–14625. https://doi.org/10.1021/acs.jpcc.2c02501.
29. **(**E. Bailey, T. J. Olin, R. M. Bricka and D. D. Adrian, A Review of Potentially Low-Cost Sorbents for Heavy Metals. *Water Research* **1999**, *33* (11), 2469–2479. https://doi.org/10.1016/s0043-1354(98)00475-8.

30. A, E. Burakov, E, V. Galunin, I, V. Burakova, A, E. Kucherova, S, Agarwal, A, G. Tkachev and V, K. Gupta, Adsorption of Heavy Metals on Conventional and Nanostructured Materials for Wastewater Treatment Purposes: A Review. *Ecotoxicology and Environmental Safety* **2018**, *148*, 702–712. https://doi.org/10.1016/j.ecoenv.2017.11.034.
31. W. S. Chai, J. Y. Cheun, P. S. Kumar, M. Mubashir, Z. Majeed, F. Banat,; S.-H. Ho and P. L. Show, A Review on Conventional and Novel Materials towards Heavy Metal Adsorption in Wastewater Treatment Application. *Journal of Cleaner Production* **2021**, *296*, 126589. https://doi.org/10.1016/j.jclepro.2021.126589.
32. T. Kamachi, T. Tatsumi, T. Toyao, Y. Hinuma, Z. Maeno, S. Takakusagi, S. Furukawa, I. Takigawa and K. Shimizu, Linear Correlations between Adsorption Energies and HOMO Levels for the Adsorption of Small Molecules on TiO2 Surfaces. *The Journal of Physical Chemistry C* **2019**, *123* (34), 20988–20997. https://doi.org/10.1021/acs.jpcc.9b05707.
33. C. Liu, Y. Li, M. Takao, T. Toyao, Z. Maeno, T. Kamachi, Y. Hinuma, I. Takigawa and K. Shimizu, Frontier Molecular Orbital Based Analysis of Solid–Adsorbate Interactions over Group 13 Metal Oxide Surfaces. *The Journal of Physical Chemistry C* **2020**, *124* (28), 15355–15365. https://doi.org/10.1021/acs.jpcc.0c04480.
34. N. Hamamoto, T. Tatsumi, M. Takao, T. Toyao, Y. Hinuma, K. Shimizu and T. Kamachi, Effect of Oxygen Vacancies on Adsorption of Small Molecules on Anatase and Rutile TiO2 Surfaces: A Frontier Orbital Approach. *The Journal of Physical Chemistry C* **2021**, *125* (7), 3827–3844. https://doi.org/10.1021/acs.jpcc.0c09614.
35. P. Pérez, R. Contreras and A. Aizman, Relationship between Solvation Energy, Chemical Potential and Hardness Variations. *Journal of Molecular Structure: THEOCHEM* **1997**, *390* (1–3), 169–175. https://doi.org/10.1016/s0166-1280(96)04771-9.
36. R. A. Miranda-Quintana and J. Smiatek, Theoretical Insights into Specific Ion Effects and Strong-Weak Acid-Base Rules for Ions in Solution: Deriving the Law of Matching Solvent Affinities from First Principles. *ChemPhysChem* **2020**, *21* (23), 2605–2617. https://doi.org/10.1002/cphc.202000644.
37. S. V. Doronin, R. A. Manzhos, A. G. Krivenko and A. P. Manzhos, Electron Transfer Kinetics of the Ferrous/Ferric Redox System on the Platinum Deposits on Gold. *Journal of Electroanalytical Chemistry* **2017**, *784*, 140–144. https://doi.org/10.1016/j.jelechem.2016.11.054.
38. S. V. Doronin, Energy of the Surface Segregation of Ag Atoms in Ag–Au Alloys in an Aqueous Solution. *Mendeleev Communications* **2020**, *30* (3), 288–290. https://doi.org/10.1016/j.mencom.2020.05.008.
39. S. V. Doronin, R. A. Manzhos and A. G. Krivenko, EDL Structure and Peculiarities of Ferricyanide Cyclic Voltammetry for Silver Deposits on Gold. *Electrochemistry Communications* **2015**, *57*, 35–38. https://doi.org/10.1016/j.elecom.2015.05.003.
40. T. Fuchigami, M. Atobe and S. Inagi, *Fundamentals and Applications of Organic Electrochemistry: Synthesis, Materials, Devices*; John Wiley & Sons, 2014, p.240
41. J. Volke and F. Liška, *Electrochemistry in Organic Synthesis*; Springer Science & Business Media, 2012, p.153.
42. M. Galiński, A. Lewandowski and I. Stępniak, Ionic Liquids as Electrolytes. *Electrochimica Acta* **2006**, *51* (26), 5567–5580. https://doi.org/10.1016/j.electacta.2006.03.016.
43. S. Zhang, N. Sun, X. He, X. Lu and X. Zhang, Physical Properties of Ionic Liquids: Database and Evaluation. *Journal of Physical and Chemical Reference Data* **2006**, *35* (4), 1475–1517. https://doi.org/10.1063/1.2204959.
44. C. Yang, J. Chen, T. Qing, X. Fan, W. Sun, A. von Cresce, M. S. Ding, O. Borodin, J. Vatamanu, M. A. Schroeder, N. Eidson, C. Wang and K. Xu, 4.0 V Aqueous Li-Ion Batteries. *Joule* **2017**, *1* (1), 122–132. https://doi.org/10.1016/j.joule.2017.08.009.

45. J. Vatamanu and O. Borodin, Ramifications of Water-in-Salt Interfacial Structure at Charged Electrodes for Electrolyte Electrochemical Stability. *The Journal of Physical Chemistry Letters* **2017**, *8* (18), 4362–4367. https://doi.org/10.1021/acs.jpclett.7b01879.
46. R. Zhang, M. Han, K. Ta, K. E. Madsen, X. Chen, X. Zhang, R. M. Espinosa-Marzal and A. A. Gewirth, Potential-Dependent Layering in the Electrochemical Double Layer of Water-in-Salt Electrolytes. *ACS Applied Energy Materials* **2020**, *3* (8), 8086–8094. https://doi.org/10.1021/acsaem.0c01534.
47. J. Han, A. Mariani, S. Passerini and A. Varzi, A Perspective on the Role of Anions in Highly Concentrated Aqueous Electrolytes. *Energy & Environmental Science* **2023**, *16* (4), 1480–1501. https://doi.org/10.1039/d2ee03682g.
48. T. R. Jow, K.Xu, O.Borodin and M. Ue, Electrolytes for Lithium and Lithium-Ion Batteries; Springer, 2014, 476. https://doi.org/10.1007/978-1-4939-0302-3
49. E. Jonsson and P. Johansson, Electrochemical Oxidation Stability of Anions for Modern Battery Electrolytes: A CBS and DFT Study. *Physical Chemistry Chemical Physics* **2015**, *17* (5), 3697–3703. https://doi.org/10.1039/c4cp04592k.
50. Y. Zhang, N. H. C. Lewis, J. Mars, G. Wan, N. J. Weadock, C. J. Takacs, M. R. Lukatskaya, H.-G. Steinrück, M. F. Toney, A. Tokmakoff and E. J. Maginn, Water-in-Salt LiTFSI Aqueous Electrolytes. 1. Liquid Structure from Combined Molecular Dynamics Simulation and Experimental Studies. *The Journal of Physical Chemistry B* **2021**, *125* (17), 4501–4513. https://doi.org/10.1021/acs.jpcb.1c02189.
51. D. Gomez Vazquez, T. P. Pollard, J. Mars, J. M. Yoo, H.-G. Steinrück, S. E. Bone, O. V. Safonova, M. F.Toney, O. Borodin and M. R. Lukatskaya, Creating Water-in-Salt-like Environment Using Coordinating Anions in Non-Concentrated Aqueous Electrolytes for Efficient Zn Batteries. Energy & Environmental Science 2023, 16 (5), 1982–1991. https://doi.org/10.1039/d3ee00205e.
52. P. Giannozzi *et al*., J. Phys. Condens. Matter 2009, **21**, 395502. https://doi.org/10.1088/0953-8984/21/39/395502
53. J. P. Perdew, K. Burke and M. Ernzerhof, Generalized Gradient Approximation Made Simple. *Physical Review Letters* **1996**, *77* (18), 3865–3868. https://doi.org/10.1103/physrevlett.77.3865.
54. G. Kresse and D. Joubert, From Ultrasoft Pseudopotentials to the Projector Augmented-Wave Method. *Physical Review B* **1999**, *59* (3), 1758–1775. https://doi.org/10.1103/physrevb.59.1758.
55. P. E. Blöchl, Projector Augmented-Wave Method. Physical Review B 1994, 50 (24), 17953–17979. https://doi.org/10.1103/physrevb.50.17953.
56. H. J. Monkhorst and J. D. Pack, Special Points for Brillouin-Zone Integrations. *Physical Review B* **1976**, *13* (12), 5188–5192. https://doi.org/10.1103/physrevb.13.5188.
57. M. Methfessel and A. T. Paxton, High-Precision Sampling for Brillouin-Zone Integration in Metals. *Physical Review B* **1989**, *40* (6), 3616–3621. https://doi.org/10.1103/physrevb.40.3616.
58. S. Grimme, J. Antony, S. Ehrlich and H. Krieg, A Consistent and Accurateab Initioparametrization of Density Functional Dispersion Correction (DFT-D) for the 94 Elements H-Pu. *The Journal of Chemical Physics* **2010**, *132* (15). https://doi.org/10.1063/1.3382344.
59. F. Neese, The ORCA Program System. *WIREs Computational Molecular Science* **2011**, *2* (1), 73–78. https://doi.org/10.1002/wcms.81.
60. A. D. Becke, Density-Functional Thermochemistry. III. The Role of Exact Exchange. *The Journal of Chemical Physics* **1993**, *98* (7), 5648–5652. https://doi.org/10.1063/1.464913.

61. J. Stephens, F.J. Devlin, C.F. Chabalowski and M.J. Frisch, Ab Initio Calculation of Vibrational Absorption and Circular Dichroism Spectra Using Density Functional Force Fields. *The Journal of Physical Chemistry* **1994**, *98* (45), 11623–11627. https://doi.org/10.1021/j100096a001.
62. V. Barone and M. Cossi, Quantum Calculation of Molecular Energies and Energy Gradients in Solution by a Conductor Solvent Model. *The Journal of Physical Chemistry A* **1998**, *102* (11), 1995–2001. https://doi.org/10.1021/jp9716997.
63. M. Cossi, V. Barone, R. Cammi and J. Tomasi, Ab Initio Study of Solvated Molecules: A New Implementation of the Polarizable Continuum Model. *Chemical Physics Letters* **1996**, *255* (4–6), 327–335. https://doi.org/10.1016/0009-2614(96)00349-1.
64. J. Tomasi, B. Mennucci and R. Cammi, Quantum Mechanical Continuum Solvation Models. *Chemical Reviews* **2005**, *105* (8), 2999–3094. https://doi.org/10.1021/cr9904009.
65. P. Tundo and M. Selva, The Chemistry of Dimethyl Carbonate. *Accounts of Chemical Research* **2002**, *35* (9), 706–716. https://doi.org/10.1021/ar010076f.
66. F. Comelli and R. Francesconi, Isothermal Vapor-Liquid Equilibria, Densities, Refractive Indices, Excess Molar Volumes, and Excess Molar Enthalpies of Dimethyl Carbonate + 1,2-Dichloroethane and + 1,1,1-Trichloroethane. *Journal of Chemical & Engineering Data* **1994**, *39* (3), 560–564. https://doi.org/10.1021/je00015a036.
67. T. M. Aminabhavi and K. Banerjee, Density, Viscosity, Refractive Index, and Speed of Sound in Binary Mixtures of Dimethyl Carbonate with Methanol, Chloroform, Carbon Tetrachloride, Cyclohexane, and Dichloromethane in the Temperature Interval (298.15−308.15) K. *Journal of Chemical & Engineering Data* **1998**, *43* (6), 1096–1101.
68. C. J. Cramer and D. G. Truhlar, A Universal Approach to Solvation Modeling. *Accounts of Chemical Research* **2008**, *41* (6), 760–768. https://doi.org/10.1021/ar800019z.
69. S. Trasatti, The Absolute Electrode Potential: An Explanatory Note (Recommendations 1986). *Pure and Applied Chemistry* **1986**, *58* (7), 955–966. https://doi.org/10.1351/pac198658070955.
70. A.H. Larsen et al, The Atomic Simulation Environment—a Python Library for Working with Atoms. *Journal of Physics: Condensed Matter* **2017**, *29* (27), 273002. https://doi.org/10.1088/1361-648x/aa680e.
71. Y.Q. Gao, Y. Georgievskii and R.A. Marcus, On the Theory of Electron Transfer Reactions at Semiconductor Electrode/Liquid Interfaces. *The Journal of Chemical Physics* **2000**, *112* (7), 3358–3369. https://doi.org/10.1063/1.480918.
72. S. V. Doronin, Y. A. Budkov and D. M. Itkis, Electrocatalytic Activity of Doped Graphene: Quantum-Mechanical Theory View. *Carbon* **2021**, *175*, 202–214. https://doi.org/10.1016/j.carbon.2021.01.020.
73. P. W. Anderson, Localized Magnetic States in Metals. *Physical Review* **1961**, *124* (1), 41–53. https://doi.org/10.1103/physrev.124.41.
74. A. S. Rosen, S. Vijay and K. A. Persson, Free-Atom-like d States beyond the Dilute Limit of Single-Atom Alloys. *Chemical Science* **2023**, *14* (6), 1503–1511. https://doi.org/10.1039/d2sc05772g. Supplementary information.
75. S. Vijay, G. Kastlunger, K. Chan and J. K. Nørskov, Limits to Scaling Relations between Adsorption Energies? *The Journal of Chemical Physics* **2022**, *156* (23). https://doi.org/10.1063/5.0096625.
76. W. Schmickler, E. Santos, M. Bronshtein and R. Nazmutdinov, Adiabatic Electron-Transfer Reactions on Semiconducting Electrodes. *ChemPhysChem* **2016**, *18* (1), 111–116. https://doi.org/10.1002/cphc.201600989.

77. E. Santos, R. Nazmutdinov and W. Schmickler, Electron Transfer at Different Electrode Materials: Metals, Semiconductors, and Graphene. *Current Opinion in Electrochemistry* **2020**, *19*, 106–112. https://doi.org/10.1016/j.coelec.2019.11.003.
78. W. Schmickler and D. Henderson, New Models for the Structure of the Electrochemical Interface. *Progress in Surface Science* **1986**, *22* (4), 323–419. https://doi.org/10.1016/0079-6816(86)90005-5.
79. R. Guidelli and W. Schmickler, Recent Developments in Models for the Interface between a Metal and an Aqueous Solution. *Electrochimica Acta* **2000**, *45* (15–16), 2317–2338. https://doi.org/10.1016/s0013-4686(00)00335-2.
80. R. R. Nazmutdinov, A. S. Berezin, G. Soldano and W. Schmickler, Orbital Overlap Effects in Electron Transfer Reactions across a Metal Nanowire/Electrolyte Solution Interface. *The Journal of Physical Chemistry C* **2013**, *117* (25), 13021–13027. https://doi.org/10.1021/jp400037g.
81. A. A. Kornyshev, A. M. Kuznetsov and J. Ulstrup, Effect of Overpotential on the Electronic Tunnel Factor in Diabatic Electrochemical Processes. *The Journal of Physical Chemistry* **1994**, *98* (14), 3832–3837. https://doi.org/10.1021/j100065a045.
82. Y. Q. Gao, Y. Georgievskii and R. A. Marcus, On the Theory of Electron Transfer Reactions at Semiconductor Electrode/Liquid Interfaces. *The Journal of Chemical Physics* **2000**, *112* (7), 3358–3369. https://doi.org/10.1063/1.480918.
83. R. R. Nazmutdinov, G. A. Tsirlina, I. R. Manyurov, M. D. Bronshtein, N.V. Titova and Z.V. Kuzminova, Misleading Aspects of the Viscosity Effect on the Heterogeneous Electron Transfer Reactions. *Chemical Physics* **2006**, *326* (1), 123–137. https://doi.org/10.1016/j.chemphys.2006.02.031.
84. Y. Q. Gao and R. A. Marcus, On the Theory of Electron Transfer Reactions at Semiconductor/Liquid Interfaces. II. A Free Electron Model. *The Journal of Chemical Physics* **2000**, *113* (15), 6351–6360. https://doi.org/10.1063/1.1309528.
85. I. G. Medvedev, Non-Local Effects in the Kinetics of Heterogeneous Charge Transfer Reactions. *Journal of Electroanalytical Chemistry* **2000**, *481* (2), 215–221. https://doi.org/10.1016/s0022-0728(99)00501-x.
86. W. Schmickler, The Surface Dipole Moment of Species Adsorbed from a Solution. *Journal of Electroanalytical Chemistry and Interfacial Electrochemistry* **1988**, *249* (1–2), 25–33. https://doi.org/10.1016/0022-0728(88)80347-4.
87. V. S. Krylov, B. B. Damaskin and V. A. Kir'yanov, The Present State and Problems of the Theory of the Kinetics of Electrode Reactions Accompanied by the Adsorption of Inactive Substances and Reagents. *Russian Chemical Reviews* **1986**, *55* (8), 706–720. https://doi.org/10.1070/rc1986v055n08abeh003217.
88. W. B. Brown and T. Y. Chang, Exact Formula for the Dipole Moment of a One-Electron Diatomic Molecule. *Proceedings of the Royal Society of London. A. Mathematical and Physical Sciences* **1985**, *401* (1821), 373–392. https://doi.org/10.1098/rspa.1985.0104.
89. J. Mitroy, M. S. Safronova and C. W. Clark, Theory and Applications of Atomic and Ionic Polarizabilities. *Journal of Physics B: Atomic, Molecular and Optical Physics* **2010**, *43* (20), 202001. https://doi.org/10.1088/0953-4075/43/20/202001.
90. C. J. Cramer and D. G. Truhlar, A Universal Approach to Solvation Modeling. *Accounts of Chemical Research* **2008**, *41* (6), 760–768. https://doi.org/10.1021/ar800019z.
91. V. S. Bryantsev, M. S. Diallo and W. A. Goddard III, Calculation of Solvation Free Energies of Charged Solutes Using Mixed Cluster/Continuum Models. *The Journal of Physical Chemistry B* **2008**, *112* (32), 9709–9719. https://doi.org/10.1021/jp802665d.

92. C. P. Kelly, C. J. Cramer and D. G. Truhlar, Aqueous Solvation Free Energies of Ions and Ion–Water Clusters Based on an Accurate Value for the Absolute Aqueous Solvation Free Energy of the Proton. *The Journal of Physical Chemistry B* **2006**, *110* (32), 16066–16081. https://doi.org/10.1021/jp063552y.
93. V. D. Parker, Energetics of Electrode Reactions. II. The Relationship between Redox Potentials, Ionization Potentials, Electron Affinities, and Solvation Energies of Aromatic Hydrocarbons. *Journal of the American Chemical Society* **1976**, *98* (1), 98–103. https://doi.org/10.1021/ja00417a017.
94. A. V. Marenich, J. Ho, M. L. Coote, C. J. Cramer and D. G. Truhlar, Computational Electrochemistry: Prediction of Liquid-Phase Reduction Potentials. *Phys. Chem. Chem. Phys.* **2014**, *16* (29), 15068–15106. https://doi.org/10.1039/c4cp01572j.
95. T. Chen and L. Dai, Carbon Nanomaterials for High-Performance Supercapacitors. *Materials Today* **2013**, *16* (7–8), 272–280. https://doi.org/10.1016/j.mattod.2013.07.002.
96. A. S. Lemine, M. M. Zagho, T. M. Altahtamouni and N. Bensalah, Graphene a Promising Electrode Material for Supercapacitors-A Review. *International Journal of Energy Research* **2018**, *42* (14), 4284–4300. https://doi.org/10.1002/er.4170.
97. P. Iamprasertkun, A. Ejigu and R. A. W. Dryfe, Understanding the Electrochemistry of "Water-in-Salt" Electrolytes: Basal Plane Highly Ordered Pyrolytic Graphite as a Model System. *Chemical Science* **2020**, *11* (27), 6978–6989. https://doi.org/10.1039/d0sc01754j.
98. R. Kumar, Su. Sahoo, E. Joanni, R. K. Singh, W. K. Tan, K. K. Kar and A. Matsuda, Recent Progress in the Synthesis of Graphene and Derived Materials for next Generation Electrodes of High Performance Lithium Ion Batteries. *Progress in Energy and Combustion Science* **2019**, *75*, 100786. https://doi.org/10.1016/j.pecs.2019.100786.
99. P. Nikitas, Theory of Electrochemically Modulated Liquid Chromatography. *Journal of Electroanalytical Chemistry* **2000**, *484* (2), 137–143. https://doi.org/10.1016/s0022-0728(00)00068-1.
100. P. Nikitas, A. Pappa-Louisi, Adsorption Isotherms for Coadsorption Studies from Solution. *Canadian Journal of Chemistry* **1986**, *64* (2), 328–332. https://doi.org/10.1139/v86-055.
101. P. Nikitas, A Unified Treatment of the Equilibrium Properties of Electrosorbed Layers Composed of Neutral and Ionic Species. *Electrochimica Acta* **1996**, *41* (14), 2159–2170. https://doi.org/10.1016/0013-4686(96)00047-3.
102. D. C. Grahame, The Electrical Double Layer and the Theory of Electrocapillarity. *Chemical Reviews* **1947**, *41* (3), 441–501. https://doi.org/10.1021/cr60130a002.
103. CRC Handbook of Chemistry and Physics, 95th Edition by William M. Haynes. CRC Press. 2014
104. J. R. Macdonald and C. A. Barlow, Work Function Change on Monolayer Adsorption. *The Journal of Chemical Physics* **1963**, *39* (2), 412–422. https://doi.org/10.1063/1.1734263.
105. S. Di Muzio, O. Palumbo, S. Brutti and A. Paolone, Thermodynamic Analysis of the Hydrolysis of Borate-Based Lithium Salts by Density Functional Theory. *Journal of The Electrochemical Society* **2022**, *169* (7), 070523. https://doi.org/10.1149/1945-7111/ac7ef2.
106. R. Younesi, G. M. Veith, P. Johansson, K. Edstrom and T. Vegge, Lithium Salts for Advanced Lithium Batteries: Li–Metal, Li–O2, and Li–S. *Energy & Environmental Science* **2015**, *8* (7), 1905–1922. https://doi.org/10.1039/c5ee01215e.
107. T. Kawamura, T. Sonoda, S. Okada and J. Yamaki, Improvement of the Stability of $LiPF_6$ Electrolytes toward Water by the Addition of LiCl. *Electrochemistry* **2003**, *71* (12), 1139–1141. https://doi.org/10.5796/electrochemistry.71.1139.

108. K. Nagayama, K. Kamioka, E. Iwata, H. Oka, Y. Tokunaga and T. Okada, The Reaction of Lithium-Manganese Oxides for the Cathode Materials of Rechargeable Lithium Batteries with Nonaqueous Electrolyte. *Electrochemistry* **2001**, *69* (1), 6–9. https://doi.org/10.5796/electrochemistry.69.6.

109. J. Wang, Y. Yamada, K. Sodeyama, C. H. Chiang, Y. Tateyama and A. Yamada, Superconcentrated Electrolytes for a High-Voltage Lithium-Ion Battery. *Nature Communications* **2016**, *7* (1), 12032. https://doi.org/10.1038/ncomms12032.

110. R. Hou, Y. Wang, Y. Sun, J. Lang, S. Yang and X. Yan, "Cation/Anion with Co-Solvation" Type High-Voltage Aqueous Electrolyte Enabled by Strong Hydrogen Bonding. *Nano Energy* **2022**, *99*, 107377. https://doi.org/10.1016/j.nanoen.2022.107377.

111. L. Suo, O. Borodin, W. Sun, X. Fan, C. Yang, F. Wang, T. Gao, Z. Ma, M. Schroeder, A. von Cresce, S. M. Russell, M. Armand, A. Angell, K. Xu, and C. Wang, Advanced High-Voltage Aqueous Lithium-Ion Battery Enabled by "Water-in-Bisalt" Electrolyte. *Angewandte Chemie International Edition* **2016**, *55* (25), 7136–7141. https://doi.org/10.1002/anie.201602397.

112. S. L. Wu, B. Z. Su, M. Z. Sun, S. Gu, Z. G. Lu, K. L. Zhang, D. Y. W. Yu, B. L. Huang, P. F. Wang, C.-S. Lee and W. J. Zhang, Dilute Aqueous-Aprotic Hybrid Electrolyte Enabling a Wide Electrochemical Window through Solvation Structure Engineering. *Advanced Materials* **2021**, *33* (41). https://doi.org/10.1002/adma.202102390.

113. H. Tomiyasu, H. Shikata, K. Takao, N. Asanuma, S. Taruta and Y.-Y. Park, An Aqueous Electrolyte of the Widest Potential Window and Its Superior Capability for Capacitors. *Scientific Reports* **2017**, *7* (1). https://doi.org/10.1038/srep45048.

114. J. Zheng, G. Tan, P. Shan, T. Liu, J. Hu, Y. Feng, L. Yang, M. Zhang, Z. Chen, Y. Lin, J. Lu, J. C. Neuefeind, Y. Ren, K. Amine, L.-W. Wang, K. Xu and F. Pan, Understanding Thermodynamic and Kinetic Contributions in Expanding the Stability Window of Aqueous Electrolytes. *Chem* **2018**, *4* (12), 2872–2882. https://doi.org/10.1016/j.chempr.2018.09.004.

115. W. Li, J. R. Dahn and D. S. Wainwright, Rechargeable Lithium Batteries with Aqueous Electrolytes. *Science* **1994**, *264* (5162), 1115–1118. https://doi.org/10.1126/science.264.5162.1115.

116. M. Sajjad, M. I. Khan, F. Cheng and W. Lu, A Review on Selection Criteria of Aqueous Electrolytes Performance Evaluation for Advanced Asymmetric Supercapacitors. *Journal of Energy Storage* **2021**, *40*, 102729. https://doi.org/10.1016/j.est.2021.102729.

117. H. Tomiyasu, H. Shikata, K. Takao, N. Asanuma, S. Taruta and Y.-Y. Park, An Aqueous Electrolyte of the Widest Potential Window and Its Superior Capability for Capacitors. *Scientific Reports* **2017**, *7* (1). https://doi.org/10.1038/srep45048.

118. E. Redondo, E. Goikolea and R. Mysyk, The Decisive Role of Electrolyte Concentration in the Performance of Aqueous Chloride-Based Carbon/Carbon Supercapacitors with Extended Voltage Window. *Electrochimica Acta* **2016**, *221*, 177–183. https://doi.org/10.1016/j.electacta.2016.10.141.

119. C. Li, S. Zhang, Y. Wang, H. Liu, T. Xing, Y. Lin, X. Rong, H. Ren, M. Wu, Q. Abbas and Z. Li, Dual Breaking of Ionic Association in Water-in-LiTFSI Electrolyte for Low Temperature Battery Applications. *Journal of Power Sources* **2022**, *544*, 231874. https://doi.org/10.1016/j.jpowsour.2022.231874.

120. B. Yang, X. Tang, W. She, D. Zhang, Y. He, B. Wang, X. Xia, Y. Li, Z. Han and K. Wang, Exploring Potassium Trifluoroacetate as a Novel Electrolyte for Enhancing Energy Density of Biomass-Derived Carbon-Based Supercapacitors and Improving Electrolyte-Electrode Adaptability. *Journal of Energy Storage* **2023**, *73*, 108805. https://doi.org/10.1016/j.est.2023.108805.

121. M. Li, H. Su, G. Zheng, U. Kuhn, N. Kim, G. Li, N. Ma, U. Pöschl and Y. Cheng, Aerosol pH and Ion Activities of HSO_4^- and SO_4 [2]$^-$ in Supersaturated Single Droplets. *Environmental Science & Technology* **2022**, *56* (18), 12863–12872. https://doi.org/10.1021/acs.est.2c01378.

122. A. Guha, M. Sahoo, K. Alam, D. K. Rao, P. Sen and T. N. Narayanan, Role of Water Structure in Alkaline Water Electrolysis. *iScience* **2022**, *25* (8), 104835. https://doi.org/10.1016/j.isci.2022.104835.

123. Z.-H. He, J.-F. Gao and L.-B. Kong, Electrolyte Effect on Electrochemical Behaviors of Manganese Fluoride Material for Aqueous Asymmetric and Symmetric Supercapacitors. *Rare Metals* **2023**, *43* (3), 1048–1061. https://doi.org/10.1007/s12598-023-02515-6.

124. K. Binnemans and P. T. Jones, Methanesulfonic Acid (MSA) in Hydrometallurgy. *Journal of Sustainable Metallurgy* **2022**, *9* (1), 26–45. https://doi.org/10.1007/s40831-022-00641-6.

125. K. Amini and M. D. Pritzker, Improvement of Zinc-Cerium Redox Flow Batteries Using Mixed Methanesulfonate-Chloride Negative Electrolyte. *Applied Energy* **2019**, *255*, 113894. https://doi.org/10.1016/j.apenergy.2019.113894.

126. Z. Li and A. W. Robertson, Electrolyte Engineering Strategies for Regulation of the Zn Metal Anode in Aqueous Zn-ion Batteries. *Battery Energy* **2022**, *2* (1). https://doi.org/10.1002/bte2.20220029.

127. T. Liu, L. Tang, H. Luo, S. Cheng and M. Liu, A Promising Water-in-Salt Electrolyte for Aqueous Based Electrochemical Energy Storage Cells with a Wide Potential Window: Highly Concentrated HCOOK. *Chemical Communications* **2019**, *55* (85), 12817–12820. https://doi.org/10.1039/c9cc05927j.

128. W. Deng, X. Wang, C. Liu, C. Li, J. Chen, N. Zhu, R. Li and M. Xue, Li/K Mixed Superconcentrated Aqueous Electrolyte Enables High-Performance Hybrid Aqueous Supercapacitors. *Energy Storage Materials* **2019**, *20*, 373–379. https://doi.org/10.1016/j.ensm.2018.10.023.

129. J. Han, H. Zhang, A. Varzi and S. Passerini, Fluorine-Free Water-in-Salt Electrolyte for Green and Low-Cost Aqueous Sodium-Ion Batteries. *ChemSusChem* **2018**, *11* (21), 3704–3707. https://doi.org/10.1002/cssc.201801930.

130. M. R. Lukatskaya, J. I. Feldblyum, D. G. Mackanic, F. Lissel, D. L. Michels, Y. Cui and Z. Bao, Concentrated Mixed Cation Acetate "Water-in-Salt" Solutions as Green and Low-Cost High Voltage Electrolytes for Aqueous Batteries. *Energy & Environmental Science* **2018**, *11* (10), 2876–2883. https://doi.org/10.1039/c8ee00833g.